Title: Structural, photocatalytic and electroconductive properties of bismuth-substituted $CaMoO_4$

Author names and affiliations:
Zoya A. Mikhaylovskaya
Zavaritsky Institute of Geology and Geochemistry, Ural Branch of the Russian Academy of Sciences
5 Ak.Vonsovskogo St., 620016, Ekaterinburg, Russia
Institute of Natural Sciences and Math, Ural Federal University
19 Mira St., 620002, Ekaterinburg, Russia
e-mail: zoya.mihaylovskaya@urfu.ru

Isaac Abrahams
Materials Research Institute, School of Biological and Chemical Sciences, Queen Mary University of London
Mile End Road, London E1 4NS, UK
e-mail: i.abrahams@qmul.ac.uk

Sofia A. Petrova
Institute for Metallurgy, Ural Branch of the Russian Academy of Sciences
101 Amundsen Str., 620016, Ekaterinburg, Russia
e-mail: danaus@mail.ru

Elena .S. Buyanova
Institute of Natural Sciences and Math, Ural Federal University
19 Mira St., 620002, Ekaterinburg, Russia
e-mail: Elena.Buyanova@urfu.ru

Nadezda V. Tarakina
Max Planck Institute of Colloids and Interfaces
Am Mühlenberg 1,14476 Potsdam, Germany
e-mail: nadja.tarakina@mpikg.mpg.de

Diana V. Piankova
Max Planck Institute of Colloids and Interfaces
Am Mühlenberg 1,14476 Potsdam, Germany
Institute of Natural Sciences and Math, Ural Federal University
19 Mira St., 620002, Ekaterinburg, Russia
e-mail: dianapyankova@gmail.com

Maria V. Morozova
Institute of Natural Sciences and Math, Ural Federal University
19 Mira St., 620002, Ekaterinburg, Russia
e-mail: maria.morozova@urfu.ru

Corresponding Author:
Zoya A. Mikhaylovskaya zoya.mihaylovskaya@urfu.ru tel: +7 343 261 7553

Abstract

The $Ca_{1-3x}Bi_{2x}\Phi_xMoO_4$ system ($0.025 \leq x \leq 0.30$, where Φ represents cation vacancies) was synthesized and studied. The $0.025 \leq x \leq 0.15$ compositions show a tetragonal defect scheelite structure. Powder X-ray and neutron diffraction patterns for compositions with $0.15 < x \leq 0.225$ exhibit a tetragonal supercell with $a_{sup} \approx \sqrt{5}a$, $c_{sup} \approx c$ where a and c are the tetragonal scheelite cell parameters. Transmission electron microscopy shows that $Ca_{0.4}Bi_{0.4}MoO_4$, crystals consist of three crystallographic domains: (1) defect scheelite; (2) tetragonal superlattice and (3) incommensurately modulated. Photocatalytic properties were studied using Rhodamine B water solutions under UV light. Catalytic activity increases with increasing Bi content. The conductivity of $0.15 < x \leq 0.225$ compositions is 10^{-7} to 10^{-8} $S \cdot cm^{-1}$ in the range 500 to 650 °C, while compositions in the range $0.025 \leq x \leq 0.15$ show conductivity values from 10^{-3} to 10^{-8} $S \cdot cm^{-1}$ from 500 to 800 °C.

KEYWORDS: A. oxides, C. X-ray diffraction, C. neutron diffraction, C. transmission electron microscopy (TEM), D. catalytic properties

1. Introduction

Scheelite-related oxides have a general formula ABO_4 and are based on a primitive cubic oxide ion array with 8-coordinate A^{n+} cations in a bisdisphenoid type of dodecahedral geometry and tetrahedral $(BO_4)^{n-}$ anions [1]. The flexibility of substitutions on both A and B sites generates a wide range of compositions, structural types and properties, leading to a variety of applications including scintillation detectors, lasers [2,3], ionic conductors [4], phosphors [5], photocatalysts [6], and microwave dielectrics [7].

In the case of substitution of divalent A^{2+} cations by trivalent M^{3+} cations, three basic charge compensation mechanisms are possible in ABO_4 scheelites:

(i) Formation of oxide ion interstitials ($A_{1-x}M_xBO_{4+x/2}$)

$$x\mathrm{A}_{\mathrm{A}}^{\mathrm{X}} \xrightarrow{\mathrm{MO}_y} x\mathrm{M}_{\mathrm{A}}^{\bullet} + \frac{x}{2}\mathrm{O}_i'' \qquad (1)$$

(ii) Co-substitution on A or B sites by subvalent cations ($A_{1-2x}M1_xM2_xBO_4$ or $A_{1-x}M1_xB_{1-x}M2_xO_4$)

$$2x\mathrm{A}_{\mathrm{A}}^{\mathrm{X}} \xrightarrow{\mathrm{M1O}_y+\mathrm{M2O}_z} x\mathrm{M1}_{\mathrm{A}}^{\bullet} + x\mathrm{M2}_{\mathrm{A}}' \qquad (2a)$$

or

$$x\mathrm{A}_{\mathrm{A}}^{\mathrm{X}} + x\mathrm{B}_{\mathrm{B}}^{\mathrm{X}} \xrightarrow{\mathrm{M1O}_y+\mathrm{M2O}_z} x\mathrm{M1}_{\mathrm{A}}^{\bullet} + x\mathrm{M2}_{\mathrm{B}}' \qquad (2b)$$

(iii) Formation of cation vacancies ($A_{1-3x}M_x\Phi_xBO_4$)

$$3x\mathrm{A}_{\mathrm{A}}^{\mathrm{X}} \xrightarrow{\mathrm{MO}_y} 2x\mathrm{M}_{\mathrm{A}}^{\bullet} + \frac{x}{2}\Phi_{\mathrm{A}}'' \qquad (3)$$

Mechanism (1) is reported for La doped $PbWO_4$ [8] and $PbMoO_4$ [9], as well as Sm doped $CaMoO_4$ [10], mechanism (2a) for Li, Sm co-doped $CaWO_4$ [11] and mechanism (2b) for Y, Sb co-doped $PbWO_4$ [12], with mechanism (3) in rare-earth substituted $Ca(Mo/W)O_4$, $Sr(Mo/W)O_4$ and $Cd(Mo/W)O_4$ [13-15]. Cation vacancies (Φ) and their ordering can have important consequences, not only on structure, but also on the physical and chemical properties. The structure of $A_{1-3x}M_{2x}\Phi_xMoO_4$ (where A and M are divalent and trivalent metal atoms, respectively) phases is often described by tetragonal symmetry (sp.gr. $I4_1/a$), but weak additional reflections present in powder diffraction patterns are often disregarded or attributed to a second phase leaving the real nature of the additional peaks unexplored.

Sleight et al. [16] first reported the $Ca_{1-3x}Bi_{2x}\Phi_xMoO_4$ solid solution with the tetragonal scheelite structure (sp. gr. $I4_1/a$) observed in the range $0.00 \leq x \leq 0.15$. More recently, *Guo* et al. [17] synthesized compositions in this solid solution in the range $0.005 \leq x \leq 0.20$, using a conventional ceramic method, and examined microstructures and microwave dielectric properties. It was shown that samples with low Bi content ($x \leq 0.015$) exhibited improved values of the microwave quality factor (Qf). The X-ray powder diffraction pattern of the $x = 0.20$ composition exhibited additional reflections, which were attributed to an unidentified secondary phase. Vibrational spectroscopy results revealed large distortions of MoO_4 and BiO_8 polyhedra [18], with a strong correlation between substitutions in the cation (A^{n+}) sublattice and microwave dielectric properties of the $Ca_{1-3x}Bi_{2x}\Phi_xMoO_4$ series [18].

While most studies to date on $Ca_{1-3x}Bi_{2x}\Phi_xMoO_4$ system have focused on their microwave dielectric properties, it is known that Bi-containing molybdates and tungstates possess a narrow band gap and exhibit high UV and VIS photocatalytic activity, mostly because of the activity of the Bi $6s^2$ valence band [19-23]. In addition, due to the relatively high energy of the band gap of $CaMoO_4$ [24-25], photocatalytic activity has been reported under UV irradiation of calcium molybdate crystals obtained by various methods. For example, data are given in [24] that $CaMoO_4$

nanocrystals exhibit photocatalytic activity for the decomposition of the dye rhodamine B (RhB) under neutral conditions. RhB dye is significantly degraded by 80% under UV illumination within 4 hours. $CaMoO_4$ nanocrystals catalyze the degradation of methylene blue [26], of tetracycline, are suitable for water splitting [27]. In addition, the conductivity properties of $Ca_{1-3x}Bi_{2x}\Phi_xMoO_4$ remain undescribed, but could significantly influence the dielectric properties. In the present work the photocatalytic and conductive properties of $Ca_{1-3x}Bi_{2x}\Phi_xMoO_4$ compositions are investigated and details of their structure revealed using transmission electron microscopy and neutron diffraction.

2. Experimental

2.1 Reagents and synthesis

Compositions of general formula $Ca_{1-3x}Bi_{2x}\Phi_xMoO_4$ ($0.025 \leq x \leq 0.275$) were synthesised by a conventional solid state method from $CaCO_3$ (99.0%, Reakhim), Bi_2O_3 (99.9%, Merck) and MoO_3 (99.5%, Reakhim). Stoichiometric amounts of dried precursors were ground in an agate mortar using ethanol as a dispersant. The dried mixtures were pelletized and heated at 500, 600, 650, 680 and 700 °C for 8 h at each step with regrinding and repelletizing every, over a total heating time ~ 40 h.

2.2 Diffraction

X-ray powder diffraction data were obtained using a Bruker Advance D8 diffractometer with a VANTEC1 detector (Ni filtered Cu-Kα radiation, θ/θ geometry). Data were collected in the 2θ range of 6-130°, with steps of 0.02103° and an effective scan time of 200 s per step.

Neutron powder diffraction data were obtained on the POLARIS diffractometer at the ISIS Facility, Rutherford-Appleton Laboratory, UK for the x = 0.05, and x = 0.20 compositions. Measurements were performed with the powdered sample contained directly in a cylindrical thin walled vanadium can (*ca.* 11 mm diameter). Data collected on back-scattering and 90° detector

banks were used in subsequent Rietveld analysis. Data sets corresponding to total proton beam currents 1080 μA h were acquired in each case.

Crystal structure refinement was carried out by Rietveld analysis with Diffrac^{Plus} TOPAS Bruker [28] using X-ray powder data, while for several compositions (x = 0.05, x = 0.10 and x = 0.20) a combination of equally weighted X-ray and back scattered neutron data sets were refined in the GSAS software suite [29]. The initial starting model for compositions in the range $0.025 \leq x \leq 0.15$ was based on the structure of the defective scheelite-related complex oxide $Sr_{0.88}Bi_{0.08}MoO_4$ [16], while that for $x > 0.15$ compositions was an ordered model derived from the basic scheelite structure of $CaWO_4$ [30]. While a single A-site exists in the basic scheelite structure, in the ordered supercell model there are two A-sites and bismuth was initially assumed to be randomly distributed across these two cation sites. However, site occupancy refinement confirmed a preferential distribution of bismuth for Bi-rich compositions and this distribution was fixed in the final refinement.

Transmission electron microscopy (TEM) was performed using a double Cs corrected JEOL JEM-ARM200F scanning transmission electron microscope, equipped with a cold-field emission gun. For the TEM study the samples were crushed in ethanol. A drop of this dispersion was put onto a copper grid covered with a holey carbon film.

2.3 Morphology investigations

Density of the homogeneous powders (ρ_{exp}) was determined with 2 ml-pycnometers with distillated water as working liquid. For porosity measurements the ceramic samples were sintered 700 °C for 12 h, weighted at air, covered with a thin layer of waterproof lacquer to make all voids «unaccessible» from the surface and weighted at air and water. Density ρ_{ceram} was determined from the hydrostatic weighing of these ceramic samples as follows:

$$\rho_{ceram}=m_{ceram}/[(m_{ceram+lacq}-m'_{ceram+lacq})/\rho_w-(m_{ceram+lacq}- m_{ceram})/\rho_{lacq}] \quad (4)$$

where m_{ceram} and $m_{ceram+lacq}$ are masses of ceramic sample and ceramic sample covered with lacquer, $m'_{ceram+lacq}$ is mass of ceramic sample covered with lacquer in water, ρ_{lacq} and ρ_w are density of lacquer and water respectively. Total porosity of ceramic samples (n) was calculated as follows:

$$n = 100\%(1-\rho_{ceram}/\rho_{exp}) \quad (5)$$

The morphology of the obtained powders was studied using a JEOL JSM 6390LA scanning electron microscope with a JED 2300 energy dispersive X-ray (EDX) detector.

2.4 Photocatalytic behaviour

The photocatalytic properties of $Ca_{1-3x}Bi_{2x}\Phi_xMoO_4$ compositions were investigated for the process of degradation of Rhodamine B (RhB) in water solution under UV irradiation. The UV experiments were conducted in a photochemical reactor made from a water jacketed quartz tube. A medium-pressure mercury vapor lamp HPL-N (Philips) of 125 W was used as an illuminating source. The lamp radiated predominantly at 365 nm corresponding to an energy of 3.4 eV. The ballast and capacitor were grouped with the lamp to avoid fluctuation of the input supply. The irradiance was measured at regular intervals using a UV-radiometer, which yielded average values of 0.022, 0.047 and 19 W m^{-2} for UV-A, UV-B and UV-C ranges, respectively. The source assembly was placed coaxially inside the water jacketed tube (ca. 200 cm^3 volume) and filled with dye solution. Water was circulated through the jacket to cool the system during the reaction. The solution temperature during the experiment was ~41±1 ˚C. The high level of oxygen in water was provided by aeration with corundum air diffuser. Constant interfusion of the solution was provided by a magnetic stirrer (~400 rpm). The RhB solution concentration was 25 ppm with a catalyst loading of 1 kg m^{-3}. Samples were taken at regular intervals (30, 60, 120, 180, 300, 600, 900, 1200, 1800 s) for subsequent analysis using a Unico 2800 spectrophotometer (552 nm). The photocatalytic degradation rate, *D*, of RhB was calculated as follows [31]:

$$D = (A_0 - A_t)/A_o \times 100\% \quad (6)$$

where A_0 and A_t are the initial absorbance (after 30 minutes in the dark) and the absorbance at irradiation time t (s), respectively. For each complex oxide photocatalytic experiment was provided at least for three times and average D values were calculated. For comparison, the activity of Degussa P25 TiO_2 catalyst (25 m^2 g^{-1}) under the same conditions was measured. Blank experiments were also carried out for RhB oxidation with and without the catalyst by visible light (24 h) and RhB oxidation with the catalyst in the dark (24 h). No significant RhB oxidation was detected under these conditions were detected.

The TOC analysis was performed in solutions after photocatytic decomposition of RhB by Walkley-Black method. Organic carbon was oxidized by 0.01 N $K_2Cr_2O_7$ solution. The reaction is assisted by the heat during 40 minutes in the presence of H_2SO_4. The excess of dichromate is titrated with ferrous sulphate with sodium diphenylamine as indicator [32].

The zero point charge pH (pH_{ZPC}) of the Bi-doped $CaMoO_4$ was measured for x=0.20 composition using the pH drift method [33]. For the pH_{ZPC} determination 20 mL of 5×10^{-2}mol/L NaCl were added to several 50 mL cylindrical high-density polystyrene flasks. A range of initial pH (pHi) values of the NaCl solutions were adjusted from 2 to 9 by adding 0.1 mol/L of HCl and NaOH. The total volume of the solution in each flask was brought to exactly 30 mL by further addition of 5×10^{-2}mol/L NaCl solution. The pH_i values of the solutions were measured and 50 mg of x=0.20 compositions were added to each flask, which was securely capped immediately. The suspensions were shaken in a shaker at 298 K and allowed to equilibrate for two days. The suspensions were filtered and the final pH (pH_f) values of the produced filtrate were recorded. The value of pH_{ZPC} was the point where the curve of (pHf–pHi) versus pH_i crosses the line equal to zero. The pH values was measured by I-160MI pH-meter.

2.5. Active species trapping experiments

To investigate the main active species in the RhB degradation process, radical scavengers were used. Ammonium oxalate, $(NH_4)_2C_2O_4$ (AO, 0.002 mol L^{-1}), t-butyl alcohol, $(CH_3)_3COH$ (TBA, 0.01 mol L^{-1}) and ascorbic acid, $C_6H_8O_6$ (AA, 0.05 mol L^{-1}) were added to RhB solution working as hole (h^+), hydroxyl radical ($^{\bullet}OH$), and superoxide radical (O_2^-) radical scavengers, respectively [34].

3.Results and Discussion

3.1 Synthesis, structure

Fig. 1 shows X-ray diffraction patterns for selected compositions in the series $Ca_{1-3x}Bi_{2x}\Phi_xMoO_4$. No second phase for $0.025 \leq x \leq 0.225$ compositions is observed. In the compositional range $0.025 \leq x < 0.15$ and all reflections can be indexed using a tetragonal scheelite model in space group $I4_1/a$. Patterns in the range $0.15 \leq x \leq 0.225$ show additional peaks (very weak for the $x = 0.15$ composition) at low angles (10-25° 2θ), which were previously attributed to a secondary phase of unknown composition [17,18]. However, as shown below, these additional peaks are actually associated with superlattice ordering of the tetragonal scheelite structure. At high bismuth concentrations ($x > 0.225$), peaks attributable to $Bi_2Mo_3O_{12}$ are observed, indicating the solid solution limit lies below this composition.

The compositional dependence of unit cell parameters for the $Ca_{1-3x}Bi_{2x}\Phi_xMoO_4$ system is shown in Fig. 2. A general increase in unit cell parameters is seen over the compositional range studied, attributable to the substitution of Ca^{2+} by larger Bi^{3+} cations with ionic radii of 1.12 and 1.17 Å, respectively [35], in agreement with previous work [17,18]. Two approximately linear ranges are seen, with a step between them at around $x = 0.15$, corresponding to the defect scheelite ($x < 0.15$) and superlattice ($x \geq 0.15$) phases evident in the diffraction data (Fig. 1). Density measurements were in good agreement with the theoretical values derived from the X-ray data (Table 1) and confirmed the formation of cation vacancies (Eq. 3).

Detail of the neutron diffraction patterns of the x = 0.05, 0.10 and 0.20 compositions are shown in Fig. 3a. The diffraction patterns of the x = 0.05 and 0.10 compositions are very similar, while that for x = 0.20 is visibly different. Most noticeable is the merging of the (211) and (114) at around 2.3 Å. Enlargement of the pattern for the x = 0.20 (Fig. 3b) composition reveals weak peaks that cannot be indexed on the tetragonal scheelite cell. These superlattice peaks, also evident in the X-ray diffraction data for compositions in the range $0.15 < x \leq 0.225$, can successfully be indexed using a tetragonal supercell of dimensions $a_{sup} = \sqrt{5}a_{sub}$, $c_{sup} = c_{sub}$ (where sup and sub denote the supercell and subcell, respectively) in the same $I4_1/a$ space group. A model structure based on ordering of the tetragonal scheelite structure was developed and refined.

Crystal and refinement parameters for the x = 0.05, x = 0.10 and x = 0.20 compositions are given in the supplementary information as Table A1, with the corresponding fitted diffraction profiles shown in Fig. A1. The refined structural parameters are given in Table 2 with significant contact distances given in Table 3.

The structural details for the x = 0.05 and x = 0.20 compositions are shown in Fig. 4. For the x = 0.20 composition, bismuth was initially assumed to be randomly distributed across the two A sites, 4b and 16f. Free refinement of the occupancies showed the 4b site to be exclusively occupied by bismuth, with the 16f site occupied by both Ca^{2+} and Bi^{3+}. The general ordering of bismuth atoms and cationic vacancies is shown in Fig. 4b.

In agreement with previous work [17,18], the x = 0.05 and 0.10 compositions exhibit slightly distorted coordination environments for the A-site cations with four short bonds (2.456 and 2.467 Å, respectively) and four slightly longer bonds (2.477 and 2.482 Å, respectively), caused by the presence of the $6s^2$ Bi^{3+} cations, as well as cationic vacancies. The Bi2 atom in the structure of the x = 0.20 composition shows a similar coordination environment, but with greater distortion, with the difference between the four short (2.405 Å) and four long (2.474 Å) bonds around 0.07 Å, reflecting the full occupancy of this site by Bi, with its stereochemically active $6s^2$ lone pair of electrons. The Ca/Bi1 site in the x = 0.20 composition, which is occupied by Ca, Bi and vacancies,

has 5 shorter bonds ranging from 2.363 to 2.464 Å and 3 longer bonds ranging from 2.615 to 2.703 Å (Fig. 4e and f)). Interestingly for the $x = 0.20$ composition, the average M-O distance for Ca/Bi1-O of 2.523 Å is significantly larger than that for the Bi2 site (2.440 Å), reflecting the greater disorder on the Ca/Bi1 site. The molybdate tetrahedra (Fig.4c and d) show little distortion in both the defect scheelite and supercell structures (Table 3), with average Mo-O distances increasing with increasing *x*-value.

During Rietveld refinement of $Ca_{0.4}Bi_{0.4}\Phi_{0.2}MoO_4$ structure, the presence of anisotropic peak broadening was noted for several sets of peaks in both X-ray and neutron powder diffraction data. In order to study the origin of this peak broadening a transmission electron microscopy study was performed. Analysis of selected-area electron diffraction (SAED) patterns of $Ca_{0.4}Bi_{0.4}\Phi_{0.2}MoO_4$ revealed the presence of three types of domains with different superstructure ordering (Fig. 5). Fig 5a shows a typical diffraction pattern obtained from domains with defect scheelite structure (with unit cell parameters $a \approx 4.9$ Å, $c \approx 10.8$ Å). Intergrowth of these domains with a second type of domain exhibiting the same superstructure ordering that was found from the powder diffraction data (with unit cell parameters $a \approx 11.1$ Å, $c \approx 10.8$ Å) is seen in Fig 5b. Fig 5c displays a similar SAED pattern, but in addition to superstructure reflections additional peaks are observed that can be described by an incommensurate modulation vector $q = -0.52*a_{sup} + 0.87*b_{sup}$. The formation of a third type of domain, with an incommensurately modulated structure, might be associated with incommensurate ordering of cations/vacancies in the Ca/Bi1 sites.

3.2 Morphology

Scanning electron microscopy (SEM) images of fracture surfaces of $Ca_{1-3x}Bi_{2x}\Phi_xMoO_4$ samples are consistent with the formation of homogenous ceramics (Fig. 6). EDX analysis shows a homogenous distribution of metals (Ca, Bi, Mo) over the samples (Fig. A2). Densitometry analysis demonstrates relatively high porosity (Table 1) of the ceramic samples which decreases with increasing bismuth concentration. It should be noted that the observed porosity values (15-28%)

were found for samples sintered at temperatures of at least 100 degrees less than the melting point. Previous work [13,15] has shown the possibility of producing high-density ceramic coatings of $Ca_{1-3x}Bi_{2x}\Phi_xMoO_4$ using melts.

3.3 Photocatalytic activity of $Ca_{1-3x}Bi_{2x}\Phi_xMoO_4$

The photocatalytic activity of several scheelite-related compounds and bismuth oxide based materials under UV and visible irradiation is reported in the literature [36-39]. In the present work the photocatalytic activity of the $Ca_{1-3x}Bi_{2x}\Phi_xMoO_4$ system was investigated for oxidation of Rhodamine B, a basic triphenylmethane dye often used as a model organic pollutant. The blank experiments show almost zero decrease of RhB concentration under visible light irradiation. Under UV irradiation (UV-A, UV-B and UV-C ranges) partial photolysis of RhB was observed. After 1800 s of irradiation, the absorption signal of RhB at 552 nm decreased by 1.4 times but the broadening of ~552 nm peak was evident. As a result the using of Eq.6 for D calculation wasn't correct. When we changed the lamp body material from quartz to glass then UV-C range of light blocked and no photolysis of RhB was observed (Fig A3). Therefore partial RhB degradation was caused only by active particles produced in water under UV-C light. However the concentration of such particles is so small that complete oxidation of RhB didn't occur. On the contrary in the case of photocatalytical oxidation no peak broadening was observed and no addition peaks at adsorption spectra were detected. This indicates a much higher concentration of active particles during photocatalytical process than during photolysis, so the degradation of RhB under of UV-C radiation on the photocatalytic process can be ignored. The final concentration of RhB after the same exposure time in the presence of Degussa P-25 is ~2.9 ppm, corresponding to a photocatalytic degradation rate of 89%. The degradation rate of RhB in the presence of $CaMoO_4$ under the same conditions is only 60%.

The $Ca_{1-3x}Bi_{2x}\Phi_xMoO_4$ compositions also show photocatalytic activity under UV irradiation, consistent with previous work, where the diffuse reflection spectrum and Kubelka–

Munk function of $Ca_{1-3x}Bi_{2x}\Phi_xMoO_4$ compositions showed optical gaps of 2.88-3.38 eV [40], indicating that the electron transition from valence to conduction bands can take place by absorbing UV light. Fig A3 shows the degradation of RhB in the presence of $Ca_{0.4}Bi_{0.4}\Phi_{0.2}MoO_4$ (x = 0.2) under UV irradiation detected by recording the decrease of the absorption at ca. λ = 552 nm. It is seen that the optical absorption intensity at 552 nm does not change with increasing irradiation time and no new absorption bands are observed. This indicates that no stable reaction intermediates are formed during the degradation process. Compared with $CaMoO_4$, the photocatalytic activities of the $Ca_{1-3x}Bi_{2x}\Phi_xMoO_4$ series are significantly enhanced (Fig 7). The degradation rates after 1800 s in the presence of x = 0.175-0.225 compositions were 71-73%. For the x = 0.25 composition, photocatalytic activity falls, probably due to the presence of the $Bi_2Mo_3O_{12}$ secondary phase observed in the XRD results.

Photocatalytic activity is seen to increase with increasing Bi content in the $Ca_{1-3x}Bi_{2x}\Phi_xMoO_4$ series, with the best photocatalytic performance achieved in the case of the x = 0.1875-0.225 compositions. Fig. 8 confirms the kinetic behavior of all compositions can be fitted according to a pesudo-first-order kinetic model, with the concentration of RhB changing according to the rate law:

$$C = C_0 \cdot \exp(-kt) \qquad (7)$$

where C is the concentration of RhB at time t, C_0 is the initial concentration of RhB and k is the reaction rate constant. The results show that reaction rates increase with Bi concentration by a factor of ~1.2.

pH effect is shown in Fig. 9a. The activity of x=0.2 composition slightly changed from pH 4.0 to 5.5 but decreased obviously at pH higher than 6.0. Solution pH can affect the surface charge of catalyst and influence $^{\bullet}OH$ radicals generation (see below). The pH_{ZPC} of x=0.2 composition is ~5.2, meaning that surface is positively charged at pH < 5.2 but negatively charged at a pH > 5.2.

Meanwhile, RhB pKa is 3.7 [41 and RhB remains a neutral molecule form at pH>3.7. Changes in the initial pH have weak influence on the contact of the pollutant and the catalyst in the range of 4<pH<5.0 but lower pH can increase the $^{\bullet}OH$ radicals generation and slightly improve the oxidation process (Fig. 9a). With the increase of initial solution pH (pH> 5.2) the repulsion force may dominant and it can decrease the mass transfer of RhB to the photocatalyst and suppress the oxidation. Such decrease of RhB oxidation with an solution pH increase is described for many oxide photocatalysts [42,43].

The degradation of the organic pollutant (RhB) proceeds via a series of parallel and consecutive reactions. Light energy equal to or higher than the band gap is absorbed by complex oxides and photogenerated electrons, e^-, and holes, h^+, can recombine or react with adsorbed species (like O_2, H_2O, OH^-, H^+) and form O_2^- and $^{\bullet}OH$ radicals. As a result, h^+, O_2^- and $^{\bullet}OH$ radicals are proposed as the active oxidative species in these systems. They can decompose RhB into degraded products or small molecules like CO_2 and H_2O. The possible reactions were initially proposed as follows [44]:

$Ca_{1-3x}Bi_{2x}\Phi_xMoO_4 + hv\ (E > Eg) \rightarrow Ca_{1-3x}Bi_{2x}\Phi_xMoO_4 + h^+ + e^-$ (generation of $h^+ + e^-$) (8)

$Ca_{1-3x}Bi_{2x}\Phi_xMoO_4 + h^+ + e^- \rightarrow Ca_{1-3x}Bi_{2x}\Phi_xMoO_4 + Q$ (recombination $h^+ + e^-$) (9)

$O_2 + e^- \rightarrow O_2^-$ (generation of O_2^-) (10)

$O_2^- + 2\ H_2O + e^- \rightarrow 2\ ^{\bullet}OH + 2\ OH^-$ (generation of $^{\bullet}OH$ from O_2^-) (11)

$h^+ + H_2O \rightarrow {}^{\bullet}OH + H^+$ (generation of $^{\bullet}OH$ from h^+) (12)

$h^+ + RhB + OH^- \rightarrow ... \rightarrow H_2O + CO_2$ (oxidation of RhB by h^+) (13)

$O_2^- + RhB + H^+ \rightarrow ... \rightarrow H_2O + CO_2$ (oxidation of RhB by O_2^-) (14)

($^{\bullet}OH + RhB + \rightarrow ... \rightarrow H_2O + CO_2$ (oxidation of RhB by $^{\bullet}OH$) (15)

In order to determine the most active species during the photodegradation process of RhB, photocatalytic reactions were performed in the presence of different radical scavengers, including

ammonium oxalate, TBA and ascorbic acid as h^+, $^\bullet OH$ and O_2^- scavengers, respectively. The photodegradation of RhB in the presence of the $x = 0.20$ composition and the mentioned scavengers is summarized in Fig 9. As shown in Fig 9b, the presence of TBA leads to a decrease in degradation rate, *D*, of around 40% after 1800 s through $^\bullet OH$ trapping. RhB degradation is also dramatically suppressed using the O_2^- scavenger, ascorbic acid, with $D \approx 6\%$ after 1800 s. In contrast, the oxidation process, is little affected in the presence of the hole scavenger, ammonium oxalate, suggesting direct oxidation of RhB by h^+ has a minimal contribution to the general oxidation process. From this it can be inferred that $^\bullet OH$ and O_2^- are the main active species during the photodegradation process. The increase in photocatalytic activity under acidic conditions shown in Fig. 9a, indicates that the $^\bullet OH$ radicals are predominantly generated from O_2^- species by Eq. 11, as previously reported for another sheelite-related compound, $PbMoO_4$ [45]. Based on these observations, a mechanism of photocatalytic degradation can be proposed and is summarized in the following reactions:

$$Ca_{1-3x}Bi_{2x}\Phi_xMoO_4 + h\nu\ (E > E_g) \rightarrow Ca_{1-3x}Bi_{2x}\Phi_xMoO_4\ + h^+ + e^- \quad (16)$$

$$Ca_{1-3x}Bi_{2x}\Phi_xMoO_4\ + h^+ + e^- \rightarrow Ca_{1-3x}Bi_{2x}\Phi_xMoO_4\ + Q\ (\text{recombination } h^+ + e^-) \quad (17)$$

$$O_2 + e^- \rightarrow O_2^- \quad (18)$$

$$O_2^- + 2\ H_2O + e^- \rightarrow 2\ ^\bullet OH + 2\ OH^- \quad (19)$$

$$O_2^- + RhB + H^+ \rightarrow ... \rightarrow H_2O + CO_2 \quad (20)$$

$$^\bullet OH + RhB + \rightarrow ... \rightarrow H_2O + CO_2 \quad (21)$$

It should be noted that in the absence of electron acceptors (O_2) or hole acceptors (H_2O), electron–hole recombination is possible and, as a result, the hydrophilicity and adsorption of O_2 on the surface of powders as well as the adsorption of the organic dye is an important aspect of the photocatalytic degradation of RhB [46]. The presence of the Bi $6s^2$ electrons can increase the hydrophilicity of the surface of the photocatalyst, while the presence of cationic vacancies and a

domain structure can provide a highly defective surface structure, leading to increased adsorption and hence greater photocatalytic activity.

Analysis of the reaction intermediates wasn't performed in the present paper. But pesudo-first-order kinetic model (also observed for TiO_2 photocatlyst [47,48]) and weak absorbance bands in the UV part of spectra (typical for dicarboxylic acids stated as intermediates in [48]) give a reason to state that RhB oxidation with Bi-doped $CaMO_4$ photocatalyst results the same intermediates. In particular oxidation process probably involves the stages of N-de-etylation, chomophore cleavage, opening ring and mineralization [47,48]. The TOC analysis showed that in the first steps of oxidation the concentration of intermediates are significant but after 10 minutes the difference between RhB and TOC concentration curves decreases (Fig 9c). In the end of oxidation process the difference between RhB and TOC concentration curves is minimal what indicates a low concentration of intermediates in solution.

Stable reuse of the photocatalyst is important for practical applications. Bi-doped $CaMO_4$ (x=0.2 composition) was collected after the photocatalytic process, washed by deionized water, dryed and reused in the same conditions for four times. The multicycles of RhB degradation is shown in Fig. 9d. After the four cycles x=0.2 composition maintained its good photocatalytic activity with a 9% decrease in removal efficiency.

In order to analyze the safety of using of materials with high Bi and Mo content such as those in the current study, possible dissolution of Bi and Mo was examined. 0.2 g of the x = 0.20 composition was dispersed in 200 mL of water for 24 h. After this time, the solution was separated from the solid and evaporated down to 25 mL. The bismuth and molybdenum contents were analyzed by atomic absorption spectroscopy. Concentrations of Bi and Mo in solution of less than 0.05 mg L^{-1}, were detected, as for standard levels in natural water. It is therefore reasonable to propose the $Ca_{1-3x}Bi_{2x}\Phi_xMoO_4$ system as photocatalysts for water purification.

3.4 Electroconductive properties of $Ca_{1-3x}Bi_{2x}\Phi_xMoO_4$

$CaMoO_4$ has been reported to be a slow mixed oxygen-ion conductor [49, 50]. The electrical conductivity of the $Ca_{1-3x}Bi_{2x}\Phi_xMoO_4$ series was investigated by a.c. impedance spectroscopy. Impedance spectra were similar for all compositions, showing semicircles with a zero high frequency intercept on the real axis. A typical impedance spectrum and model equivalent circuit are shown in Fig.10. The equivalent circuit consists of a parallel combination of a resistor (R) and a capacitor (C), as in the study of (Ca/Sr/Ba)MoO_4 [50]. The capacitance value was found to be $\sim 10^{-11}$ F, corresponding to the total resistance of the electrolyte [51]. The separation of the total resistance into bulk and grain boundary components was not possible.

Arrhenius plots of total conductivity and the compositional variation of conductivity at 873 K for the $Ca_{1-3x}Bi_{2x}\Phi_xMoO_4$ series are presented in Fig. 11. The Arrhenius plots are generally linear, with slight deviation from linearity caused by kinetic restraints at low temperatures. The conductivity of $CaMoO_4$ is in good agreement with that found by Petrov and Kofstad [49] and Maji *et al*. [50]. All compositions show increased conductivity in comparison to $CaMoO_4$. Ionic transport in the $Ca_{1-3x}Bi_{2x}\Phi_xMoO_4$ system assumes the presence of interstitial oxygen positions, although these have not been identified by diffraction methods [52]. The activation energy for $x < 0.15$ compositions changes little in this compositional range (1.4-1.6 eV), indicating that the charge carriers and conduction mechanism in $Ca_{1-3x}Bi_{2x}\Phi_xMoO_4$ is the same as in the parent compound $CaMoO_4$ [50]. The conductivity of in $Ca_{1-3x}Bi_{2x}\Phi_xMoO_4$ at 873 K increases with increasing Bi content up to $x = 0.15$, but then shows a sharp decrease between $x = 0.15$ and 0.175.

It should be noted that since compositions with high dopant concentration ($x \geq 0.15$) show a decrease in melting point temperature, the maximum measurement temperature for these compositions was only 923 K (Fig. 11b). For these high x-value compositions, the activation energy values are lower (0.9-1.1 eV) compared to those for the lower x-value compositions, suggesting a change in the charge carriers and/or a change in conduction mechanism. The decrease in conductivity and activation energy above ca. $x = 0.15$ correlates with the appearance of superlattice reflections seen in the diffraction data. The lowering of conductivity in the ordered structure is

attributed to the trapping of charge carriers and is a common feature of order-disorder type transitions. The decrease in activation energy in the superlattice ordered compositions might be caused by a lowering of the migration energy due by cationic ordering, with the O^{2-} ion migration pathways close to Bi^{3+} cations likely to be more energetically favourable due to the high polarizability of the Bi $6s^2$ lone pair of electrons.

4. Conclusions

A cation vacancy solid solution is formed in the system $Ca_{1-3x}Bi_{2x}\Phi_xMoO_4$ in the compositional range $0.0 \leq x \leq 0.225$. Phases in the range $0.025 \leq x \leq 0.15$ show a tetragonal scheelite structure, isostructural with $CaMoO_4$, while in the range $0.15 < x < 0.225$ a tetragonal superstructure is seen with $a_{sup} = \sqrt{5}a_{sub}$, $c_{sup} = c_{sub}$. The microstructure of the Bi rich compositions is complex and made up of an intergrowth of three different types of domains: domains with the defect scheelite structure, domains with tetragonal superstructure and domains with additional incommensurately modulated ordering.

The photocatalytic activity of $Ca_{1-3x}Bi_{2x}\Phi_xMoO_4$ compositions is significantly greater than that of the parent compound $CaMoO_4$ and increases with increasing Bi content. This is attributed not only to the presence of Bi in the phases, but also to cationic vacancies and the domain structure. $^{\bullet}OH$ and O_2^- are found to be the main active species during the photodegradation process.

Conductivity increases with increasing *x*-value up to $x = 0.15$. A maximum value of $1.14 \cdot 10^{-5}$ S cm^{-1} at was achieved at 973 K for the $x = 0.15$ composition. Higher *x*-value compositions all show lower conductivities attributed to charge carrier trapping in the ordered superlattice.

Acknowledgments

The study was done with a support of RSF, projects № 20-73-10048. The travel grant for neutron diffraction work was given by Act 211 Government of the Russian Federation, contract № 02.A03.21.0006. The authors are grateful to the Science and Technology Facilities Council STFC

for neutron beam time at the ISIS facility, Rutherford Appleton Laboratory, award No. RB1910306. Dr Ron Smith at ISIS is thanked for his help in neutron data collection.

References

[1] A.F. Wells Structural Inorganic Chemistry 5th Ed.,Oxford Science Publications, 1984

[2] V. B. Mikhailik, H. Kraus, G. Miller, M. S. Mykhaylyk, D. Wahl, Luminescence of $CaWO_4$, $CaMoO_4$, and $ZnWO_4$ scintillating crystals under different excitations, J. Appl. Phys. 97 (2005) 083523. http://dx.doi.org/10.1063/1.1872198

[3] N. Faure, C. Borel, M. Couchaud, G. Basset, R. Templier, C. Wyon, Optical properties and laser performance of neodymium doped scheelites $CaWO_4$ and $NaGd(WO_4)_2$, Appl. Phys. B: Lasers Opt., 63 (1996) 593–598.

https://doi.org/10.1007/BF01830998

[4] N. Sharma, K. M. Shaju, G. V. S. Rao, B. V. R. Chowdari, Z.L. Dong, T. J. White, Carbon-coated nanophase $CaMoO_4$ as anode material for Li ion batteries, Chem. Mater. 16 (2004) 504–512. http://dx.doi.org/10.1021/cm0348287

[5] L. S. Cavalcante, V. M. Longo, J. C. Sczancoski, M. A. P. Almeida, A. A. Batista, J. A. Varela, M. O. Orlandi, E. Longo, M. S. Liu, Electronic structure, growth mechanism and photoluminescence of $CaWO_4$ crystals, Cryst. Eng. Comm. 14 (2012) 853–868.

http://dx.doi.org/10.1039/C1CE05977G

[6] W. F. Yao, J. H. Ye, Photophysical and photocatalytic properties of $Ca_{1-x}Bi_xV_xMo_{1-x}O_4$ solid solutions, J. Phys. Chem. B 110 (2006) 11188–11195.

http://dx.doi.org/10.1021/jp0608729

[7] G. K. Choi, J. R. Kim, S. H. Yoon, K. S. Hong, Microwave dielectric properties of scheelite (A = Ca, Sr, Ba) and wolframite (A = Mg, Zn, Mn) $AMoO_4$ compounds, J. Eur. Ceram. Soc. 27 (2007) 3063–3067.

https://doi.org/10.1016/j.jeurceramsoc.2006.11.037

[8] T. Esaka, T. Mina-ai., H. Iwahara, Oxide ion conduction in the solid solution based on the scheelite-type oxide $PbWO_4$, Solid State Ion. 57 (1992) 319–325. https://doi.org/10.1016/0167-2738(92)90165-L

[9] G. G. Zhang, Q. F. Fang, X. P. Wang, Z. G. Yi, Dielectric relaxation study of $Pb_{1-x}La_xMoO_{4+\delta}$ (x = 0–0.3) oxide-ion conductors, J. Phys.: Condens. Matter. 15 (2003) 4135–4142. https://doi.org/10.1088/0953-8984/15/24/307

[10] J. Cheng, C. Liu, W. Cao, M. Qi, G. Shao, Synthesis and electrical properties of scheelite $Ca_{1-x}Sm_xMoO_{4+d}$ solid electrolyte ceramics, Mater. Res. Bull. 46 (2011) 185–189. https://doi.org/10.1016/j.materresbull.2010.11.019

[11] X. Yang, Y. Wang, N. Wang, S. Wang, G. Gao, Effects of co-doped Li^+ ions on luminescence of CaWO4:Sm^{3+} nanoparticles, J. Mater. Sci.: Mater. Electronics 25 (2014) 3996–4000 https://doi.org/10.1007/s10854-014-2119-4

[12] J. Xie,, P. Yang, H. Yuan, J. Liao, B. Shen, Z. Yin, D. Cao, M. Gu, Influence of Sb and Y co-doping on properties of $PbWO_4$ crystal, J. Cryst. Growth 275 (2005) 474–480 https://doi.org/10.1016/j.jcrysgro.2004.12.028

[13] M. M. Haque, D.-K. Kim, Luminescent properties of Eu^{3+}activated $MLa_2(MoO_4)_4$ based (M=Ba, Sr and Ca) novel red-emitting phosphors, Mater. Lett. 63 (2009) 793−796. http://dx.doi.org/10.1016/j.matlet.2009.01.018

[14] P. Jiang, W. Gao, R. Cong, T. Yang, Structural investigation of the A-site vacancy in scheelites and the luminescence behavior of two continuous solid solutions $A_{1-1.5x}Eu_x\square_{0.5x}WO_4$ and $A_{0.64-0.5y}Eu_{0.24}Li_y\square_{0.12-0.5y}WO_4$ (A = Ca, Sr; □ = vacancy), Dalton Trans. 44 (2015) 6175−6183. http://dx.doi.org/10.1039/c5dt00022j

[15] E. Tomaszewicz, S. M. Kaczmarek, H. Fuks, New cadmium and rare-earth metal molybdates with scheelite type structure, Mater. Chem. Phys. 122 (2010) 595−601. https://doi.org/10.1016/j.matchemphys.2010.03.052

[16] J. A. W. Sleight, K. Aykan, New nonstoichiometric molybdate, tungstate, and vanadate catalysts with the scheelite-type structure, J .Solid State Chem. 13 (1975) 231−236.
https://doi.org/10.1016/0022-4596(75)90124-3

[17] J. Guo, C. A. Randall, G. Zhang, D. Zhou, Y. Chen, H. Wang, Synthesis, structure, and characterization of new low-firing microwave dielectric ceramics: $Ca_{1-3x}Bi_{2x}\Phi_xMoO_4$, J. Mater. Chem. C 2 (2014) 7364−7372.
http://dx.doi.org/10.1039/c4tc00698d

[18] J. Guo, C. A. Randall, D. Zhou, G. Zhang, C. Zhang, B. Jin, H. Wang, Correlation between vibrational modes and dielectric properties in $Ca_{1-3x}Bi_{2x}\Phi_xMoO4$ ceramics, J. Europ. Ceram. Soc. 35 (2015) 4459–4464.
https://doi.org/10.1016/j.jeurceramsoc.2015.08.020

[19] B. Muktha, G. Madras, T. N.Guru Row, A novel scheelite-like structure of BaBi2Mo4O16: Photocatalysis and investigation of the solid solution, BaBi2Mo4−xWxO16 ($0.25 \leq x \leq 1$), J. Photoch. Photobio. A. 15 (2007) 177-185
https://doi.org/10.1016/j.jphotochem.2006.10.016

[20] W. Yao, J. Ye, Photophysical and photocatalytic properties of $Ca_{1-x}Bi_xV_xMo_{1-x}O_4$ solid solutions, J. Phys. Chem. B. 110 (2006) 11188-11195
https://doi.org/10.1021/jp0608729

[21] B. Muktha, T. N.Guru Row, Effect of substitution in the scheelite-like series, $A_xBa_{1-x}Bi_2Mo_4O_{16}$ (A = Ca, Sr, Pb), Mater. Res. Bull. 42 (2007) 2150-2155
https://doi.org/10.1016/j.materresbull.2007.01.012

[22] R. He, S. Cao, P. Zhou, J. Yu, Recent advances in visible light Bi-based photocatalyst, Chin. J. Catal. 35 (2014) 989-1007
https://doi.org/10.1016/S1872-2067(14)60075-9

[23] J. Yu, J. Xiong, B. Cheng, Y. Yu, J. Wang. Hydrothermal preparation and visible-light photocatalytic activity of Bi_2WO_6 powders, J. Solid State Chemistry 178 (2005) 1968–1972

https://doi.org/10.1016/j.jssc.2005.04.003

[24] H. Chanchal, S. Tuhin, V. A. Aswin, M. Venkataramanan. Bilayer stabilized Ln^{3+}-doped $CaMoO_4$ nanocrystals with high luminescence quantum efficiency and photocatalytic properties, Dalton Trans. 43 (2014) 6623–6630

https://doi.org/10.1039/c3dt53450b

[25] A. P. Marques, V. M. Longo, D.M.A. de Melo, P. S. Pizani, E. R. Leite, J. A. Varela, E. Longo. Shape controlled synthesis of $CaMoO_4$ thin films and their photoluminescence property, J. Solid State Chemistry 181 (2008) 1249‑ 1257

https://doi.org/10.1016/j.jssc.2008.01.051

[26] M. Kusuma, G.T. Chandrappa. Effect of calcination temperature on characteristic properties of$CaMoO_4$ nanoparticles, J. Sci. – Adv.Mater. Dev. 4 (2019) 150-157

https://doi.org/10.1016/j.jsamd.2019.02.003

[27] A. M. Huerta-Flores, I. Juárez-Ramírez, L. M. Torres-Martínez, J. E. Carrera-Crespo, T. Gómez-Bustamante, O. Sarabia-Ramos. Synthesis of $AMoO_4$ (A = Ca, Sr, Ba) photocatalysts and their potential application for hydrogen evolution and the degradation of tetracycline in water, J. Photoch. Photobio. A 356 (2018) 29–37

https://doi.org/10.1016/j.jphotochem.2017.12.029

[28] $Diffrac^{Plus}$: Topas Bruker AXS GmbH, Ostliche. Rheinbruckenstraße 50, D-76187, Karlsruhe, Germany. 2009

[29] Larson AC, Von Dreele RB (2004) General Structure Analysis System (GSAS). Los Alamos National Laboratory Report LAUR-86-748

[30] M. I. Kay, B. C. Frazer, I. Almodovar, Neutron diffraction refinement of $CaWO_4$. J. Chem. Phys. 40 (1964) 504-506.

https://doi.org/10.1063/1.1725144

[31] M. Kang, J. Liang, F. Wang, X. Chen, Y. Lu, J. Zhang, Structural design of hexagonal/monoclinic WO_3 phase junction for photocatalytic degradation, Mater. Res. Bull. 121 (2020) 110614
https://doi.org/10.1016/j.materresbull.2019.110614
[32] Z. Aregahegn Optimization of the analytical method for the determination of organic matter, J. Soil Sci. Environ. 11, 1 (2020) 1-5
https://doi.org/10.5897/JSSEM2019.0784
[33] M. El Haddad, R.Mamouni, N. Saffaj, S. Lazar, Removal of a cationic dye – Basic Red 12 – from aqueous solution by adsorption onto animal bone meal, J. Assoc. Arab Univ. Basic Appl. Sci. 12 (2012), 48–54
http://dx.doi.org/10.1016/j.jaubas.2012.04.003
[34] M.A.I. Molla, I. Tateishi, M. Furukawa, H. Katsumata, T. Suzuki, S. Kaneco, Evaluation of reaction mechanism for photocatalytic degradation of dye with self-sensitized TiO_2 under visible light irradiation, Open J. Inorg. Non-Metallic Mater., 07 (2017) 1-7.
https://doi.org/10.4236/ojinm.2017.71001
[35] R. D. Shannon, Revised effective ionic radii and systematic studies of interatomic distances in halides and chalcogenides, Acta Cryst. A 32 (1976) 751–767.
http://doi.org/10.1107/S0567739476001551
[36] B.Muktha, G. Madras, T. N. Guru Row, A novel scheelite-like structure of $BaBi_2Mo_4O_{16}$: Photocatalysis and investigation of the solid solution, $BaBi_2Mo_{4-x}W_xO_{16}$ ($0.25 \leq x \leq 1$),
J. Photochem. Photobiol. A: Chem., 187 (2007) 177-185.
https://doi.org/10.1016/j.jphotochem.2006.10.016
[37] S. Martha, P. C. Sahoo, K. M. Parida, An overview on visible light responsive metal oxide based photocatalysts for hydrogen energy production, RSC Adv., 5 (2015) 61535 —61553.
https://doi.org/10.1039/C5RA11682A

[38] H. Kou, J. Gao, Z. S. Li, Z. G. Zou, Research on photocatalytic degradation properties of organics with different new photocatalysts, Current Organic Chem., 14 (2010), 728 –744
https://doi.org/10.2174/138527210790963430

[39] W. Yao, J.Ye, Photophysical and photocatalytic properties of $Ca_{1-x}Bi_xV_xMo_{1-x}O_4$ solid solutions, J. Phys. Chem. B 2006, 110 (2006) 11188–11195.
https://doi.org/10.1021/jp0608729

[40] R. A. Parulin, I. V. Timoshenko, Yu A Kuznetsova, A. F. Zatsepin, E. S. Buyanova, Z A Mikhaylovskaya, Optical properties and energy band parameters of luminescent CaMoO4:Bi ceramics, J. Phys.:Conf. Ser. 1124 (2018) 051005.
https://doi.org/10.1088/1742-6596/1124/5/051005

[41] A.A. Inyinbor, F.A. Adekola and G.A. Olatunji, Adsorption of rhodamine B dye from aqueous solution on irvingia gabonensis biomass: kinetics and thermodynamics studies, S. Afr. J. Chem. 68 (2015), 115–125.

[42] K.Rokesh, A. Nithya, K. Jeganathan, K. Jothivenkatachalam, A Facile solid state synthesis of cone-like ZnO microstructure an efficient solar-light driven photocatalyst for rhodamine B degradation, Mater. Today, 3 (2016), 4163–4172
https://doi.org/10.1016/j.matpr.2016.11.091

[43] H.-J. Cui, H.-Z. Huang, B. Yuan, M.-L.Fu, Decolorization of RhB dye by manganese oxides: effect of crystal type and solution pH, Geochem.Trans., 16 (2015) 10
https://doi.org/10.1186/s12932-015-0024-2

[44] A. Zaleska-Medynska, Metal Oxide-Based Photocatalysis, 1st ed., Elsevier, 2018
https://doi.org/10.1016/C2016-0-01872-7

[45] D.B.Hernández-Uresti, A.Martínez-de la Cruz, J.A.Aguilar-Garib, Photocatalytic activity of PbMoO4 molybdate synthesized by microwave method, Catal. Today 212 (2013) 70–74
http://dx.doi.org/10.1016/j.cattod.2012.12.015

[46] M.Hashim, C.Hu, X.Wang, X.Li, D.Guo, Synthesis and photocatalytic property of lead molybdate dendrites with exposed (001) facet, Appl. Surf. Sci. 258 (2012) 5858–5862 http://dx.doi.org/10.1016/j.apsusc.2012.02.116

[47] A. Akbar Isari, A. Payan, , M.Fattahi, , S. Jorfi, B. Kakavandi, Photocatalytic degradation of Rhodamine B and Real Textile Wastewater using Fe-Doped TiO2 anchored on Reduced Graphene Oxide (Fe-TiO2/rGO): Characterization and feasibility, mechanism and pathway studies. Appl. Surf. Sci. 462 (2018) 549–564 http://dx.doi.org/10.1016/j.apsusc.2018.08.133

[48] Z. He, S. Yang, Y. Ju, C. Sun, Microwave photocatalytic degradation of rhodamine B using TiO_2 supported on activated carbon: Mechanism implication. J. Environ. Sci., 21(2009) 268–272. http://dx.doi.org/10.1016/s1001-0742(08)62262-7

[49] A. Petrov, P. Kofstad, Electrical conductivity of $CaMoO_4$, J. Solid State Chem. 30 (1979) 83–88. https://doi.org/10.1016/0022-4596(79)90133-6

[50] B. K. Maji, H. Jena , R. Asuvathraman, K. V. Govindan Kutty, Electrical conductivity and thermal expansion behavior of MMoO4 (M = Ca, Sr and Ba), J. Alloys Comp. 640 (2015) 475–479 http://dx.doi.org/10.1016/j.jallcom.2015.04.054

[51] J.T.S.Irvine., D.C.Sinclair, A.R. West, Electroceramics: characterization by impedance spectroscopy, Adv. Mat. 2 (1990) 132-138. http://dx.doi.org/10.1002/adma.19900020304

[52] T. Esaka, Ionic conduction in substituted scheelite-type oxides, Solid State Ion. 136–137 (2000) 1-9 https://doi.org/10.1016/S0167-2738(00)00377-5

Figure capture list

Fig. 1. X-ray powder diffraction pattern of the $Ca_{1-3x}Bi_{2x}\Phi_xMoO_4$ series. Stars indicate superstructural reflections, diamonds mark $Bi_2Mo_3O_{12}$ phase reflections. Enlagements of patterns in the 2theta range 10-30° are shown in the inset

Fig. 2. Variation of the unit cell parameters for $Ca_{1-3x}Bi_{2x}\Phi_xMoO_4$ with x (for $0.15<x\leq0.225$ nominal parameters $V'=V/5$ and $a'=a/\sqrt{5}$ were used)

Fig. 3. Detail of the neutron diffraction patterns of the x = 0.05, 0.10 and 0.20 compositions (a) and enlargement of the pattern for the x = 0.20 (b)\

Fig. 4 Structure details of $Ca_{1-3x}Bi_{2x}\Phi_xMoO_4$. {(a, (c), (f)} x = 0.05 and {(b), (d), (f)} figures are for x = 0.2. {(a), (b)} figures are projections on *(xoy)* plane, {(c),(d)} and {(e), (f)} figures show coordination of Mo and Bi respectively

Fig. 5. (a-e) Selected area electron diffraction patterns of $Ca_{0.4}Bi_{0.4}\Phi_{0.2}MoO_4$ recorded along different zone axes. Indexing in white denotes the basic scheelite structure, red indices denote the superstructure obtained from X-ray powder diffraction, and the incommensurately modulated pattern is indexed in blue. (f) Relation between basic-sheelite sublattice and superstructure lattice obtained from X-ray powder diffraction

Fig. 6 SEM images of fracture surfaces of a ceramic pellet of x=0.2 composition: (a) - secondary electrons imaging ; (b) - backscattering electrons imaging, scale 1:2000

Fig. 7 Time (a) and composition (b) dependences of conversion degree for $Ca_{1-3x}Bi_{2x}\Phi_xMoO_4$; (c) absorption spectra of RhB in different irradiation time in the presence of x=0.2 composition

Fig.8 Kinetic curves of RhB oxidation under UV light with $Ca_{1-3x}Bi_{2x}\Phi_xMoO_4$ catalysts, reaction rate constants k (s^{-1}) are shown

Fig 9. Variation of degradation rates of RhB degradation by x=0.2 composition (a) in the resence of radical scavengers (b) at different pH; (c) relative concentration of TOC and RhB in solutions during oxidation (photocatalyst is x=0.2 composition) (d) relative concentration of RhB during recycling photocatalyst (x=0.2 composition)

Fig. 10. Typical impedance spectrum for $Ca_{1-3x}Bi_{2x}\Phi_xMoO_4$ (x=0.075 composition, T=923 K, symbols), model circuits and model spectrum (line))

Fig. 11. Arrhenius plots of total conductivity of $Ca_{1-3x}Bi_{2x}\Phi_xMoO_4$ (a,b); the plots of conductivity *vs* dopant concentration for $Ca_{1-3x}Bi_{2x}\Phi_xMoO_4$ series(c)

Table1

Table 1. Results of densitometry for $Ca_{1-3x}Bi_{2x}\Phi_xMoO_4$ series. $\rho_{X\text{-}ray}$ is the theoretical density based on the crystal structure, ρ_{exp} is experimental density measured by pycnometry on powders, ρ_{ceram} is the experimental density from the hydrostatic weighing of ceramic samples. Porosity = $100\%(\rho_{X\text{-}ray}-\rho_{ceram})/\rho_{X\text{-}ray}$

x	$\rho_{X\text{-}ray}$, g/cm^3	ρ_{exp} ±0.02, g/cm^3	ρ_{ceram}	Porosity %
0.025	4.40	4.36	3.17	28
0.050	4.55	4.56	3.56	22
0.075	4.69	4.68	3.79	19
0.100	4.83	4.81	3.94	19
0.125	4.97	4.92	3.97	20
0.150	5.10	5.09	4.20	18
0.175	5.21	5.19	4.47	14
0.1875	5.28	5.23	4.62	12
0.200	5.34	5.36	4.71	13
0.2125	5.41	5.40	4.75	12

Table2

Table 2. Final refined structural parameters for $Ca_{1-3x}Bi_{2x}\Phi_xMoO_4$ at 20 °C. Estimated standard deviations are given in parentheses.

(a) x = 0.05

Atom	Site	x	y	z	Occ.	U_{iso} (Å^2)
Ca/Bi	4b	0.0	0.25	0.625	0.85/0.10	0.00893(8)
Mo	4a	0.0	0.25	0.125	1.0	0.00679(6)
O	16f	0.14838(4)	0.00723(5)	0.20913(2)	1.0	0.01147(5)

(b) x = 0.10

Atom	Site	x	y	z	Occ.	U_{iso} (Å^2)
Ca/Bi	4b	0.0	0.25	0.625	0.70/0.20	0.01048(9)
Mo	4a	0.0	0.25	0.125	1.0	0.00794(7)
O	16f	0.14857(4)	0.00788(5)	0.20886(2)	1.0	0.01391(6)

(c) x = 0.20

Atom	Site	x	y	z	Occ.	U_{iso} (Å^2)
Ca1/Bi1	16f	0.4037(5)	-0.0495(5)	0.3644(3)	0.50/0.25	0.0110(3)
Bi2	4b	0.0	0.25	0.625	1.0	0.0110(3)
Mo1	4a	0.5	0.25	0.375	1.0	0.0105(3)
Mo2	16f	0.3007(3)	0.1544(3)	0.6186(2)	1.0	0.0105(3)
O1	16f	0.1729(4)	0.1590(4)	0.7035(3)	1.0	0.0171(2)
O2	16f	0.2862(4)	0.0258(4)	0.5492(3)	1.0	0.0171(2)
O3	16f	0.1036(4)	0.1817(4)	0.4614(3)	1.0	0.0171(2)
O4	16f	0.3204(3)	0.2659(3)	0.5262(2)	1.0	0.0171(2)
O5	16f	0.4890(3)	0.1204(3)	0.4531(3)	1.0	0.0171(2)

Table3

Table 3. Significant contact distances (Å) for $Ca_{1-3x}Bi_{2x}\Phi_xMoO_4$ at 20 °C. Estimated standard deviations are given in parentheses.

(a) x = 0.05

Ca/Bi-O	2.4561(2) × 4	**Ca/Bi-O′**	2.4766(2) × 4	**Mo-O**	1.7740(2) × 4
(b) x = 0.10					
Ca/Bi-O	2.4671(3) × 4	**Ca/Bi-O′**	2.4816(2) × 4	**Mo-O**	1.7749(3) × 4
(c) x = 0.20					
Ca/Bi1-O1	2.449(6)	**Ca/Bi1-O2**	2.460(7)	**Ca/Bi1-O2′**	2.712(6)
Ca/Bi1-O3	2.415(7)	**Ca/Bi1-O4**	2.363(6)	**Ca/Bi1-O4′**	2.703(7)
Ca/Bi1-O5	2.464(6)	**Ca/Bi1-O5′**	2.615(5)	**Bi2-O1**	2.474(4) × 4
Bi2-O3	2.405(3) × 4	**Mo1-O5**	1.781(3) × 4	**Mo2-O1**	1.803(5)
Mo2-O2	1.724(5)	**Mo2-O3**	1.886(5)	**Mo2-O4**	1.714(5)

Figure 1

Click here to download high resolution image

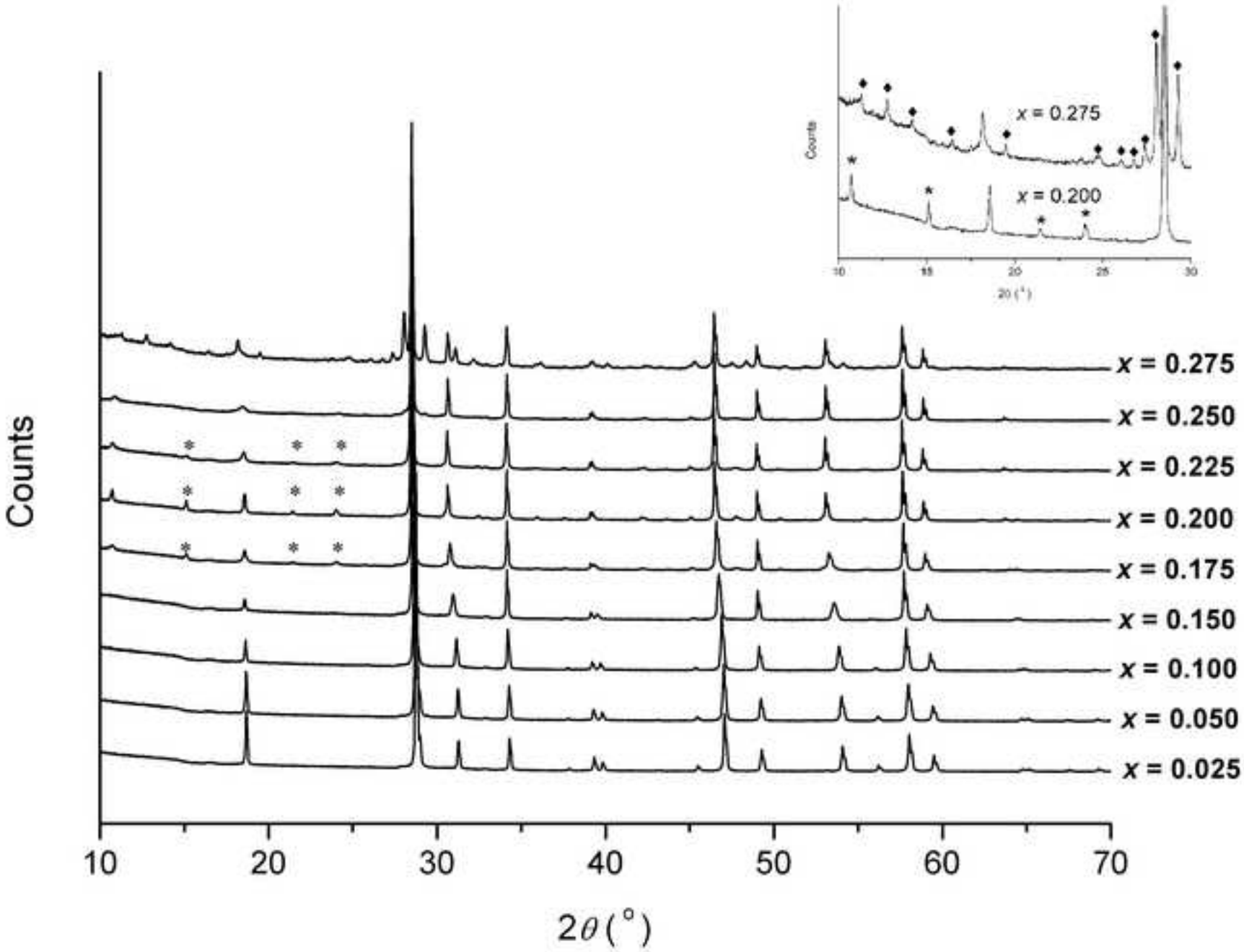

Figure 2

Click here to download high resolution image

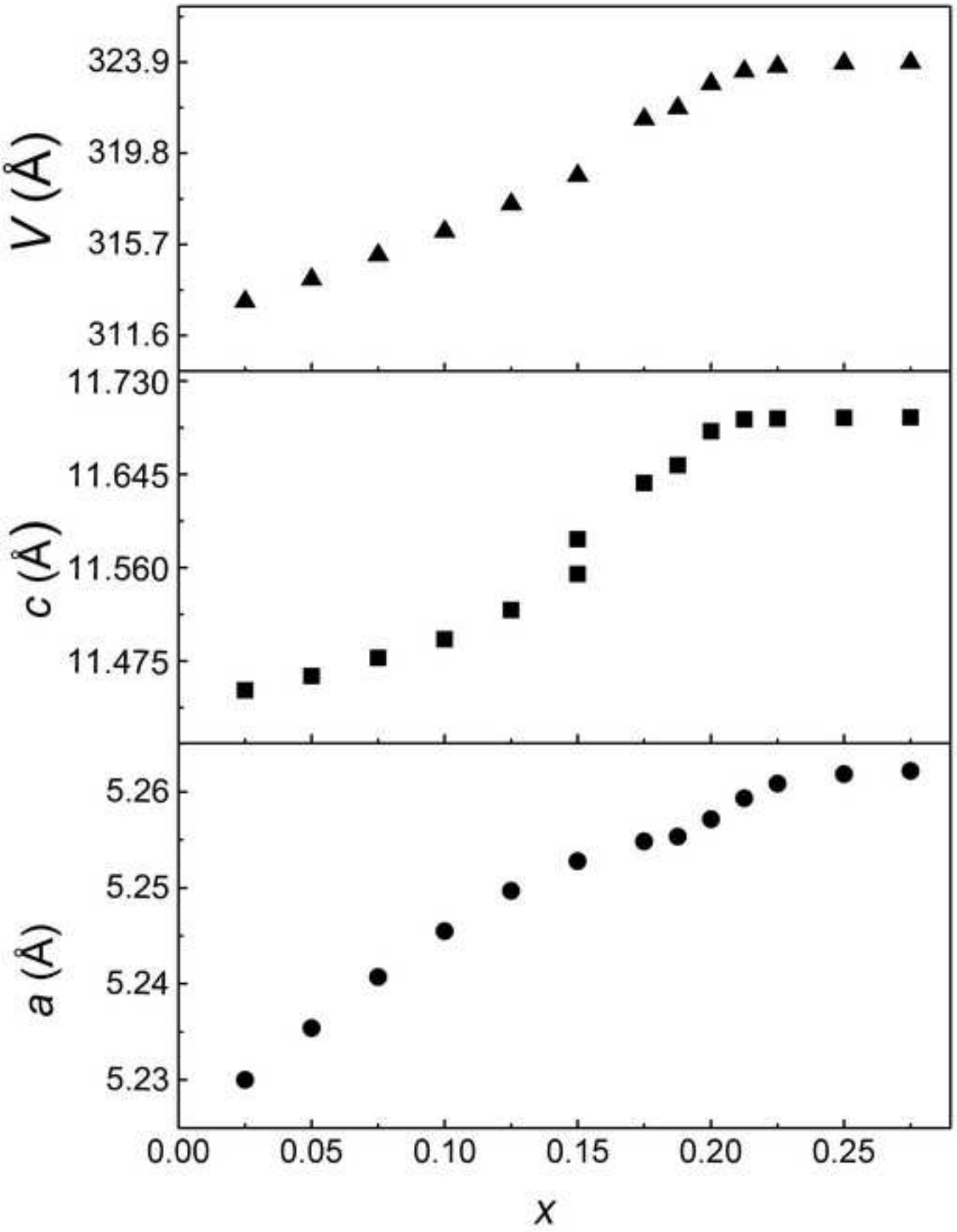

Figure 3

Click here to download high resolution image

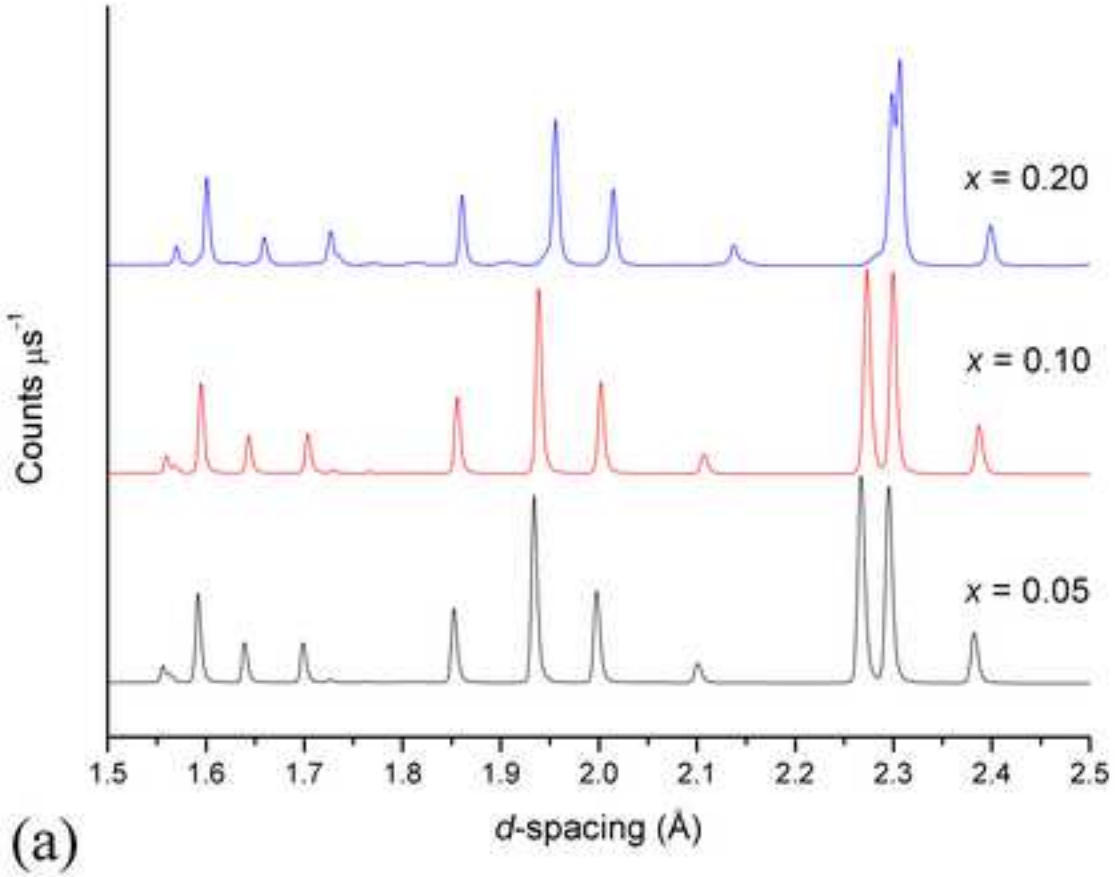

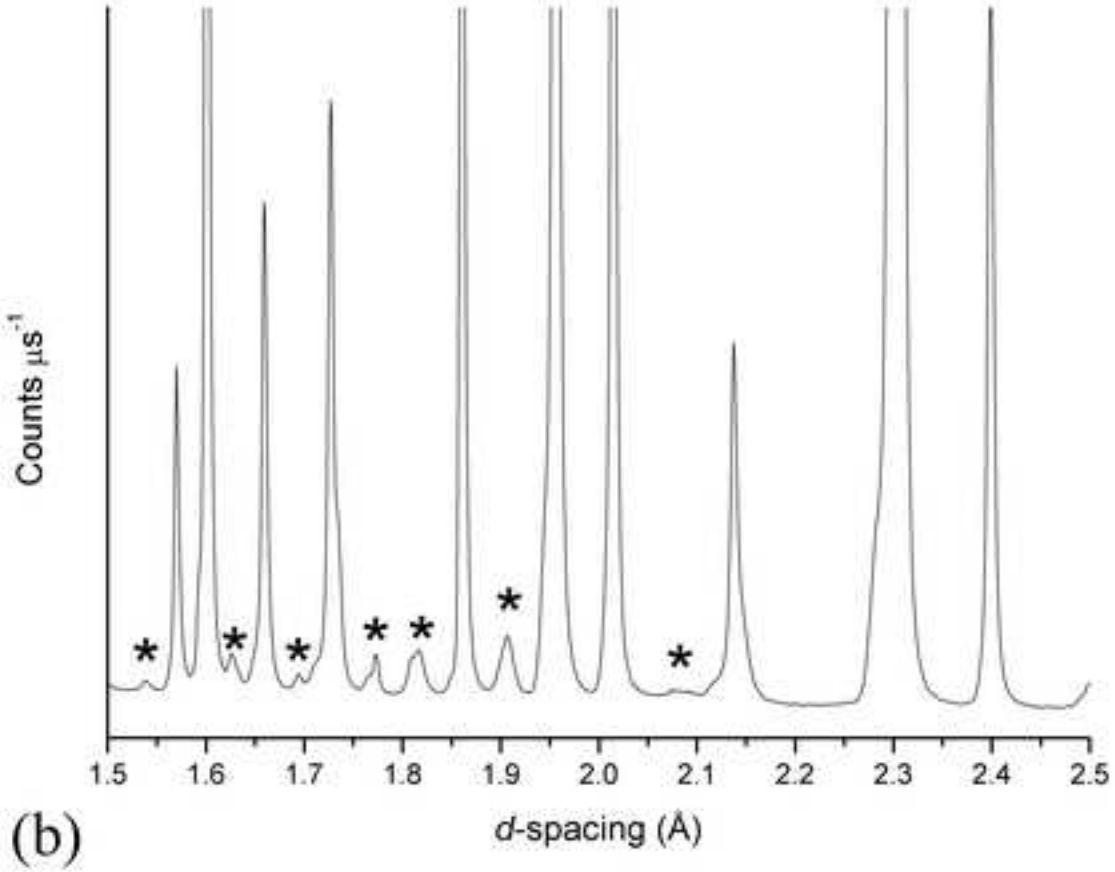

Figure 4

Click here to download high resolution image

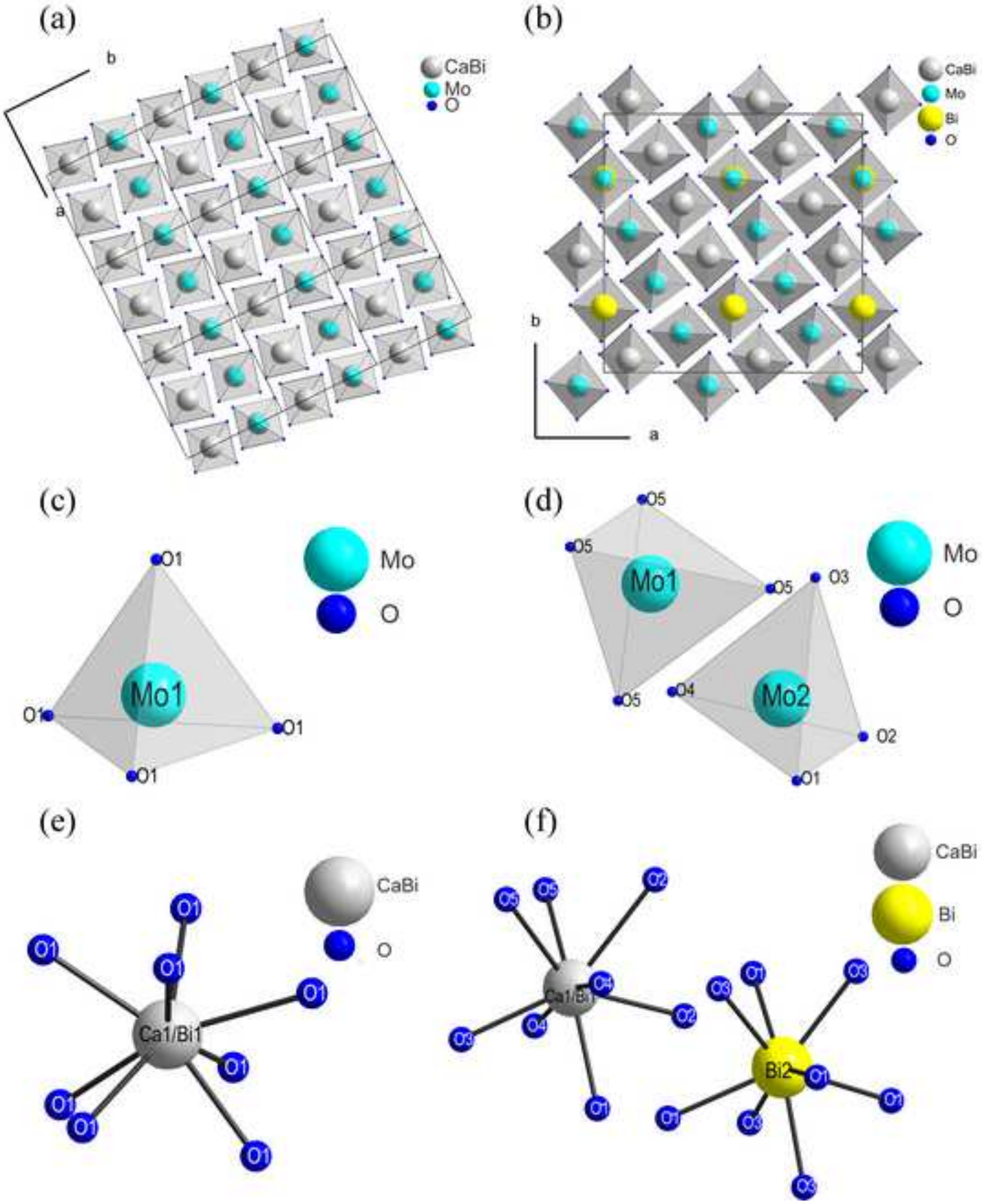

Figure 5

Click here to download high resolution image

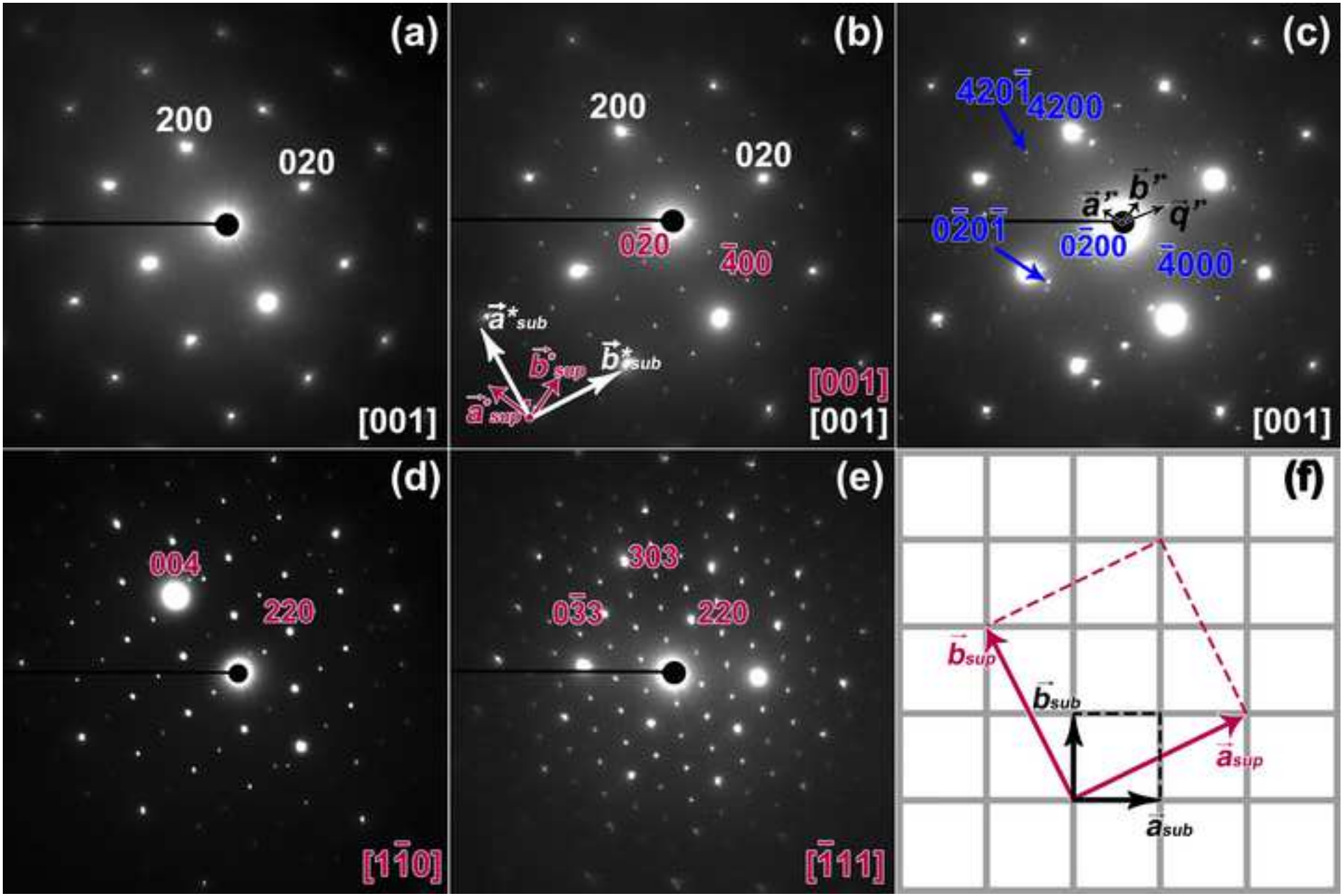

Figure 6

Click here to download high resolution image

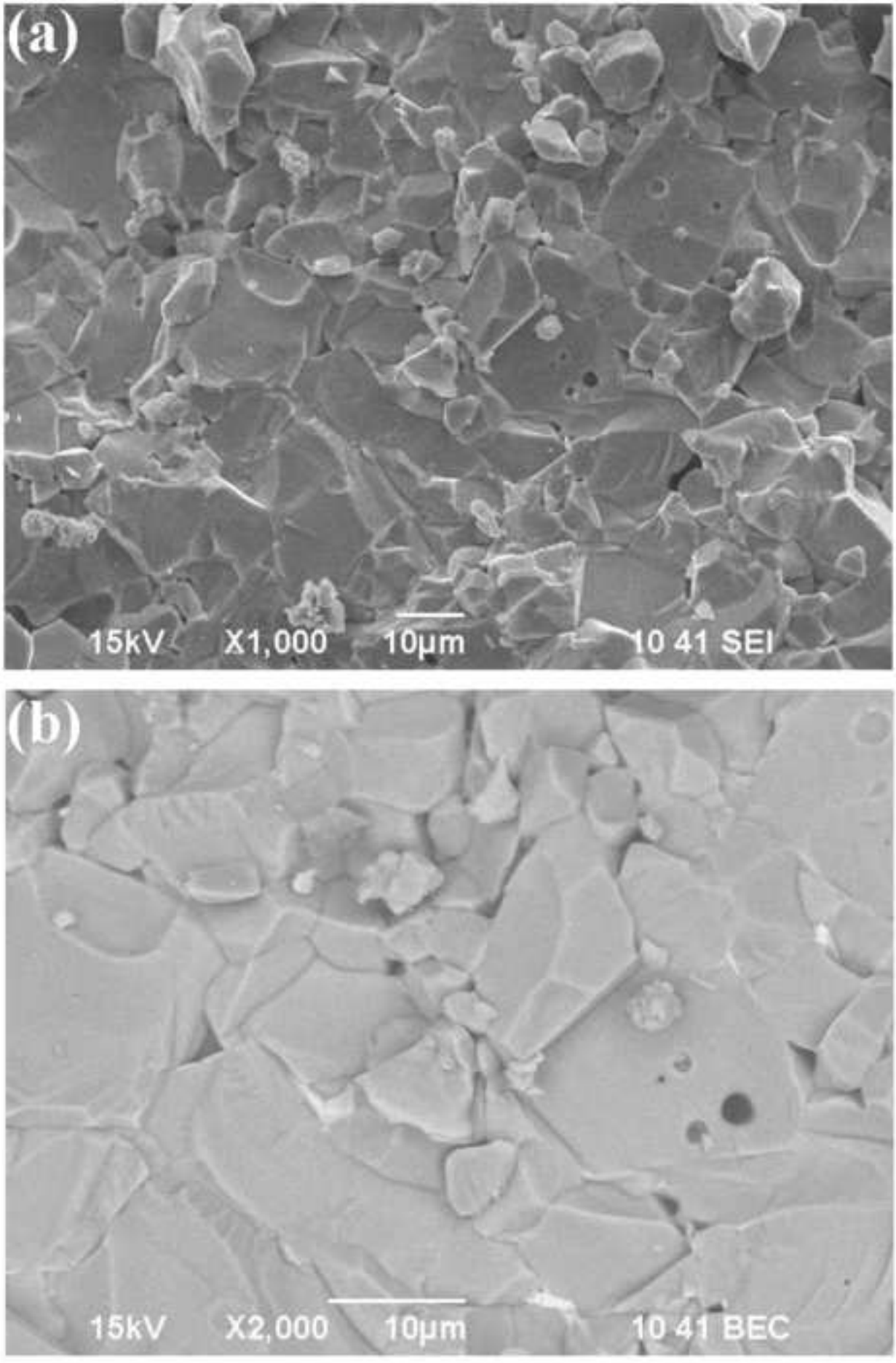

Figure 7

Click here to download high resolution image

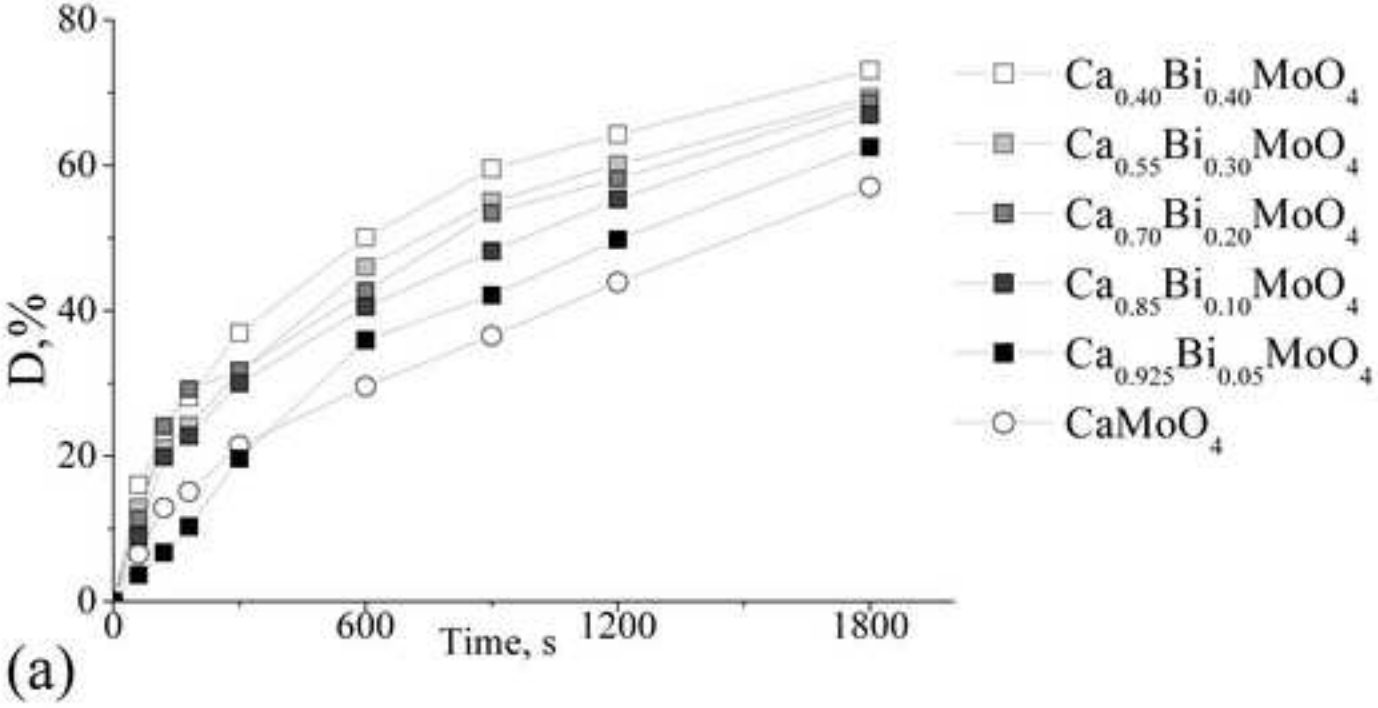

(a)

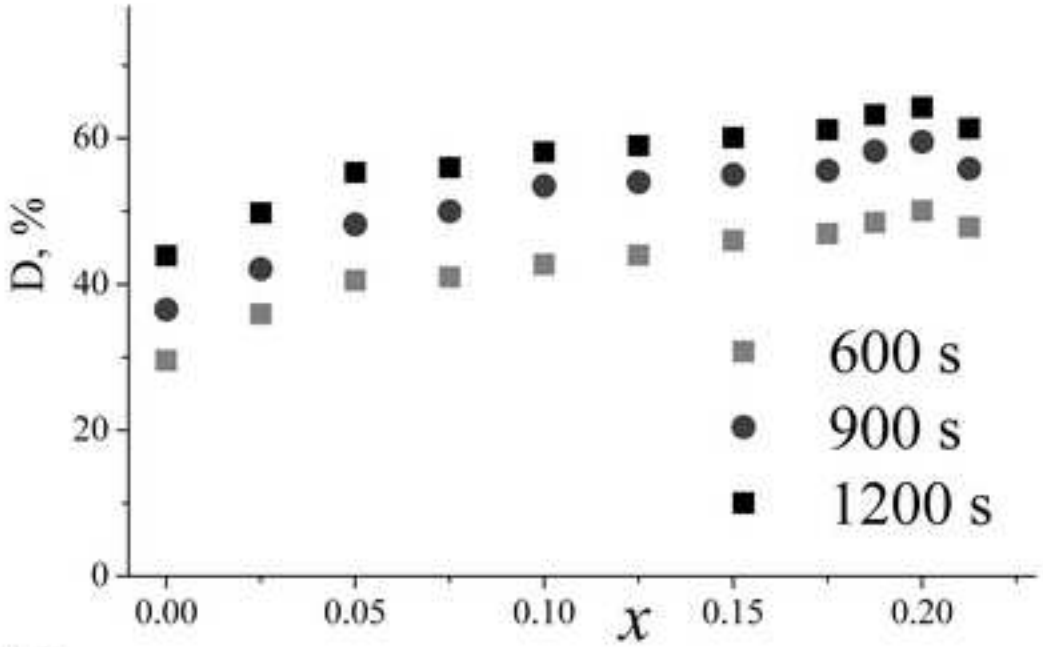

(b)

Figure 8

Click here to download high resolution image

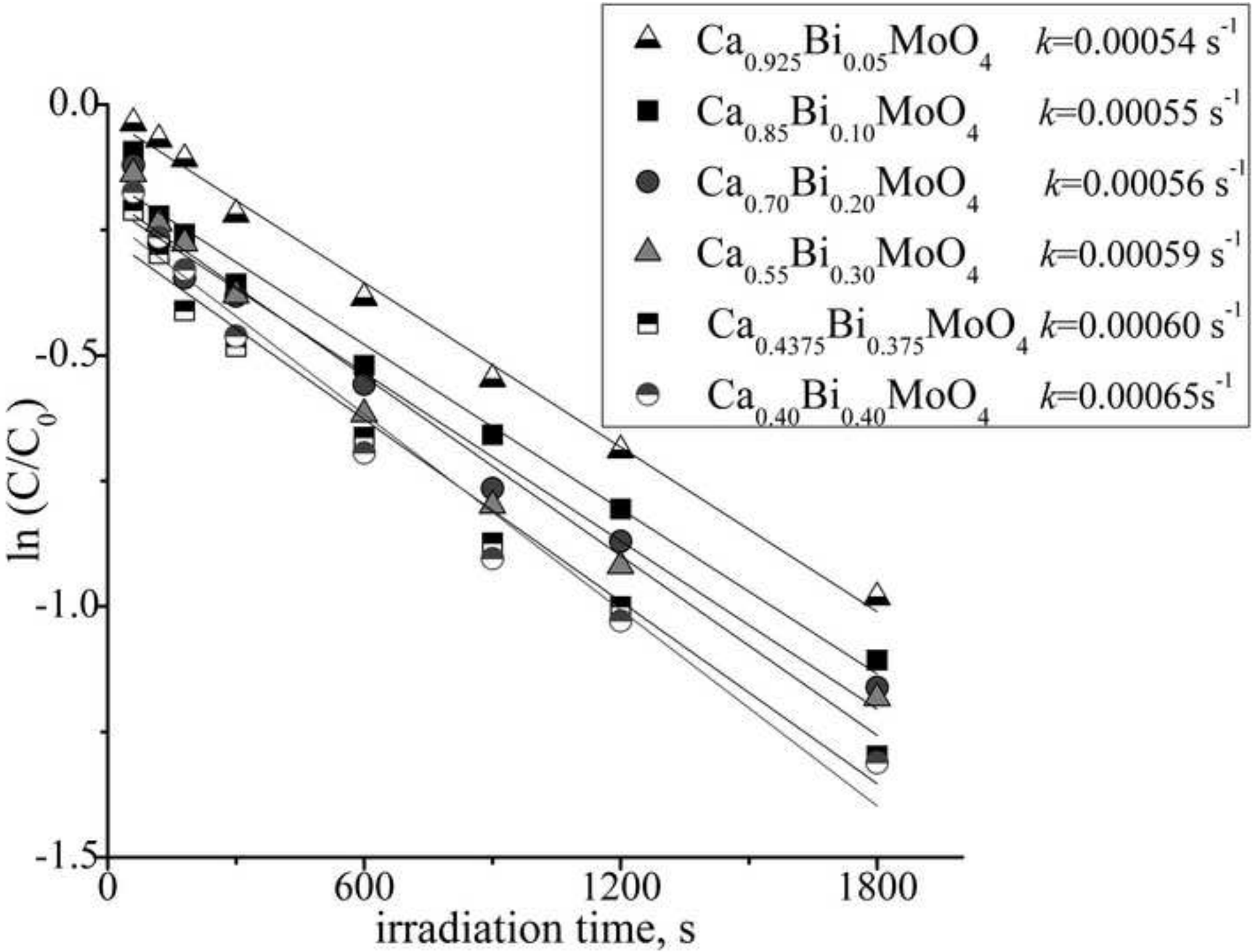

Figure 9

Click here to download high resolution image

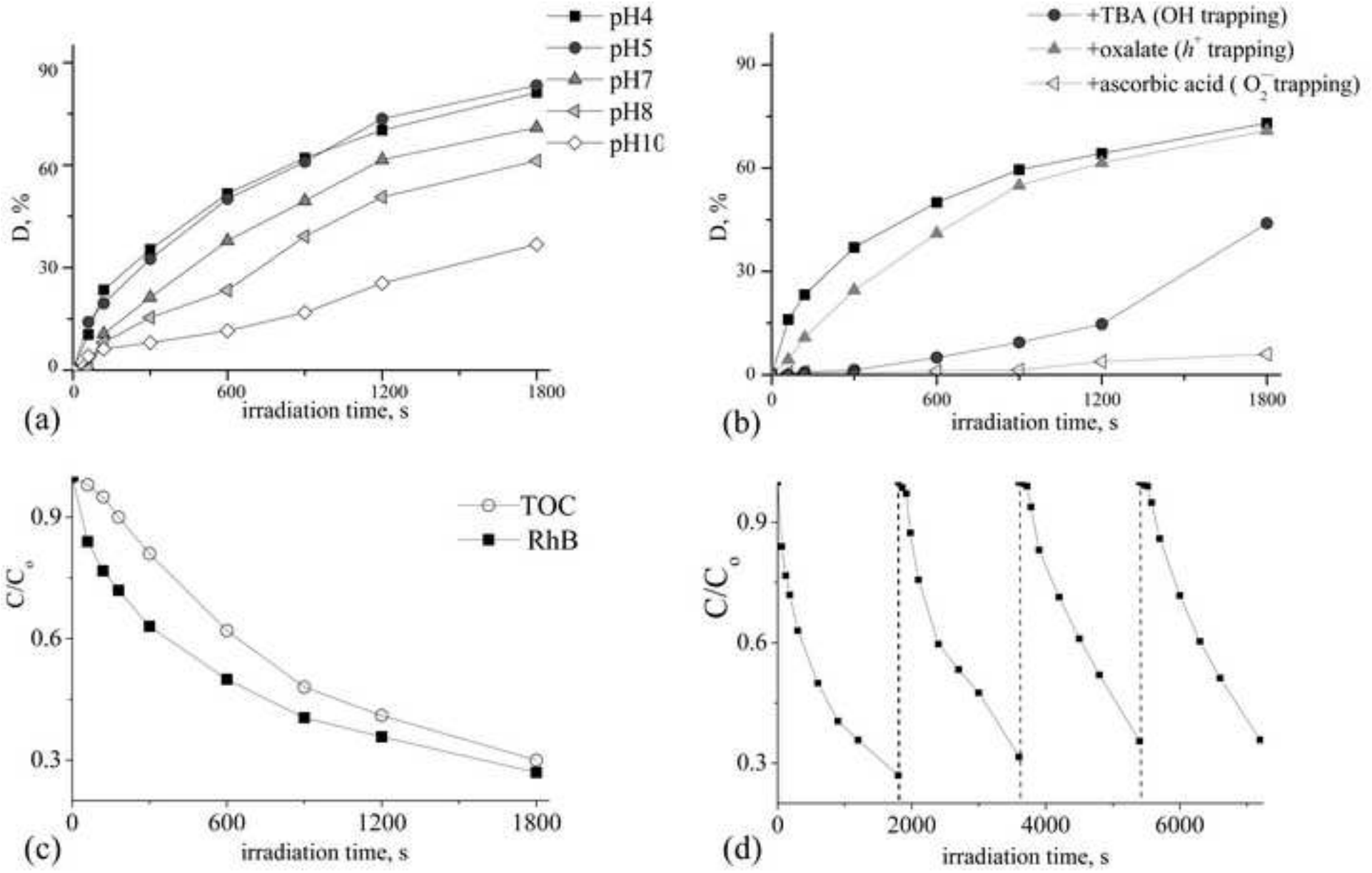

Figure 10

Click here to download high resolution image

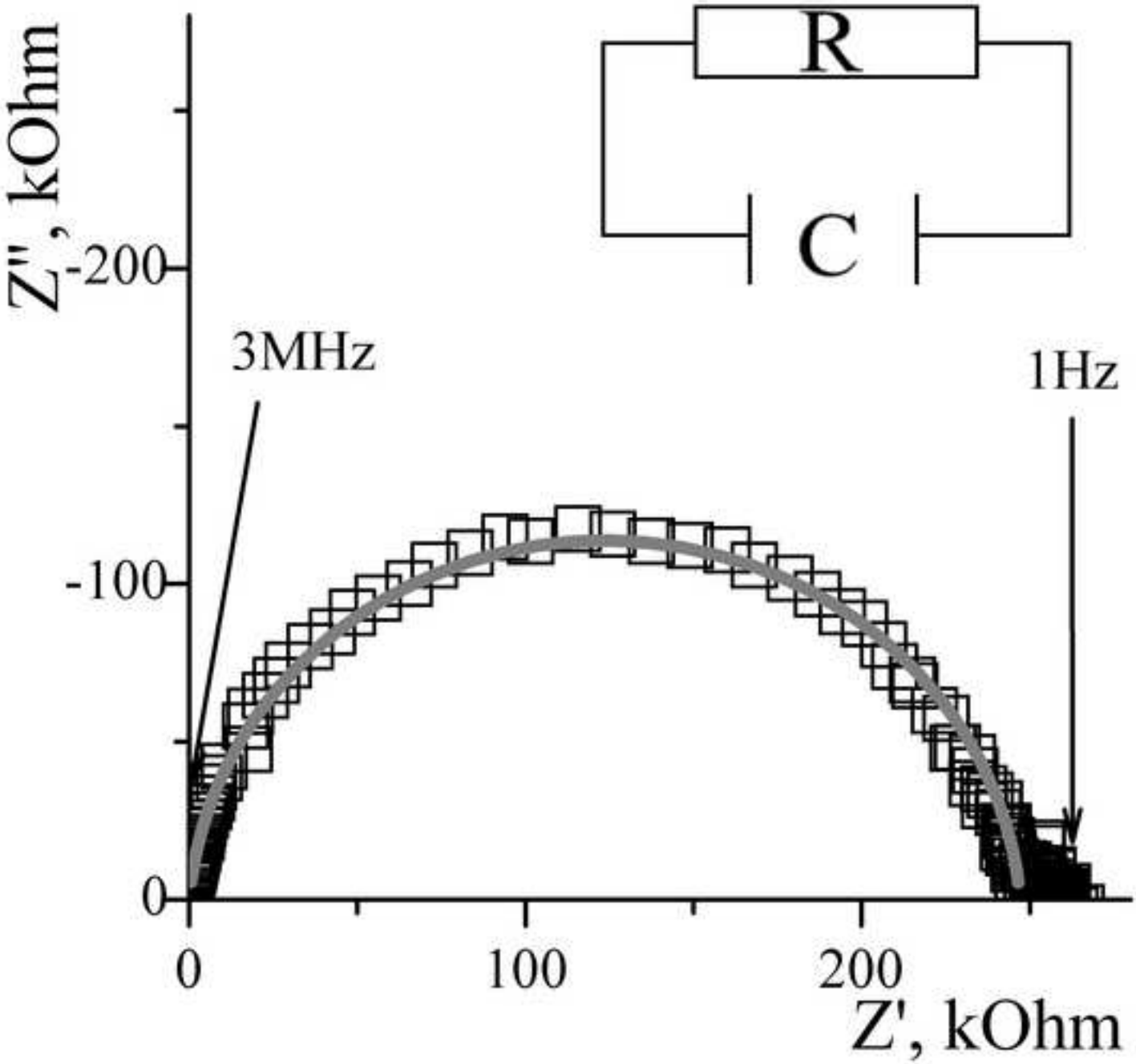

Figure 11

Click here to download high resolution image

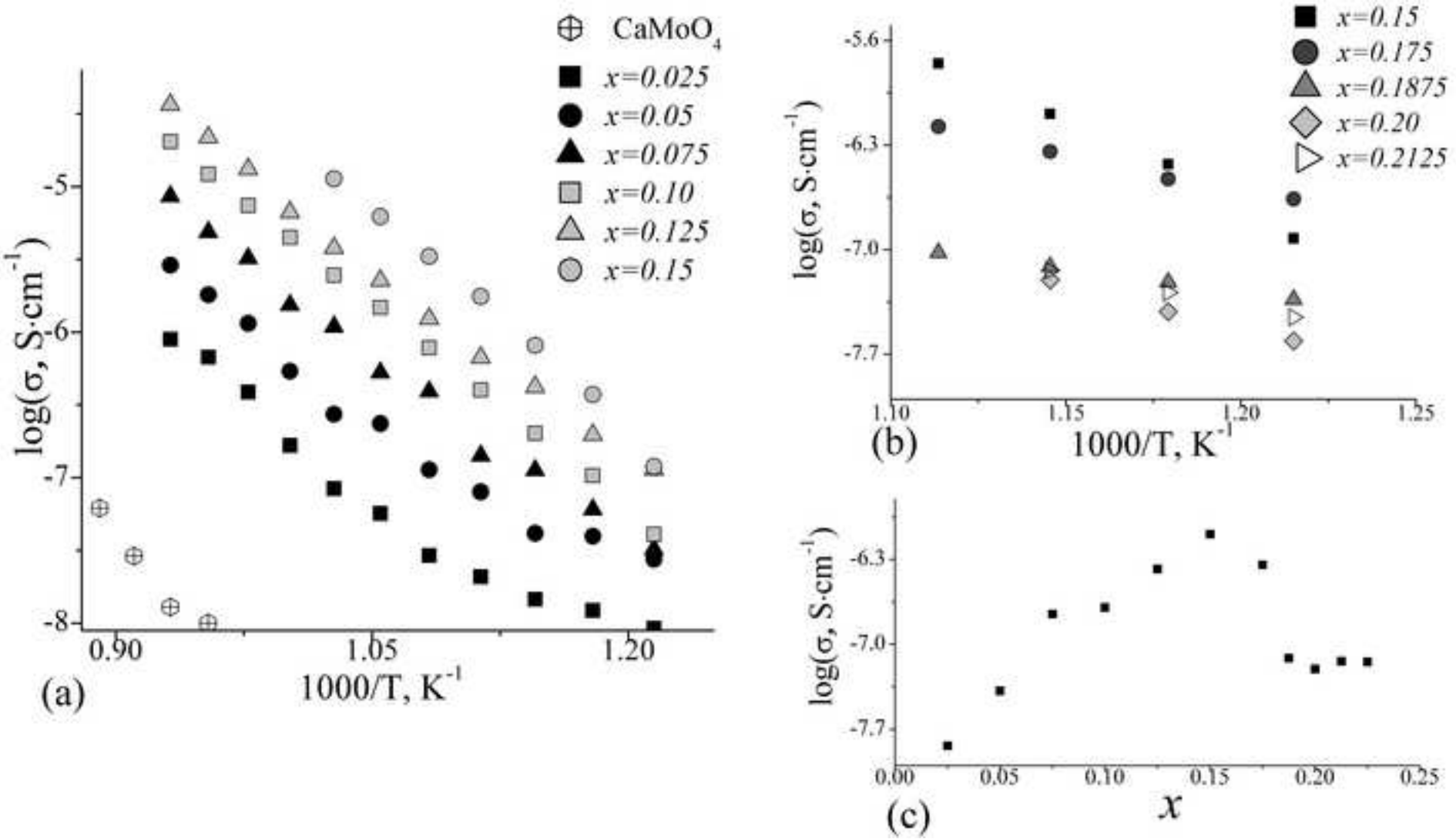

Highlights

$Ca_{1-3x}Bi_{2x}\Phi_xMoO_4$ ($0.025 \leq x \leq 0.15$) shows a defect scheelite structure

$Ca_{1-3x}Bi_{2x}\Phi_xMoO_4$ ($0.15 < x \leq 0.225$) exhibits a supercell with $a_{sup} \approx \sqrt{5}a$, $c_{sup} \approx c$

Three types of domains in $Ca_{0.4}Bi_{0.4}MoO_4$ microcrystals were found by TEM

The photocatalytic activity of $Ca_{1-3x}Bi_{2x}\Phi_xMoO_4$ for RhB oxidation increases with x